ABSTRACT

Title of Dissertation: MEASURING INTERFACE EFFECTS IN SOLID-STATE BATTERIES

Karl Dale Larson, Doctor of Philosophy, 2025

Dissertation Directed by: Assistant Professor Paul Albertus Chemical and Biomolecular Engineering

Solid-state batteries with solid metal anodes would be a promising solution for improved energy storage. However, the unstable behaviors of solid-solid interfaces impedes implementation. Further study of these interfaces, both at the planar solid metal anode | electrolyte interface and the grain | grain interface in solid electrolytes is necessary to elucidate practical engineering techniques to improve cycling stability. We assemble three-electrode symmetric cells of Sodium | Sodium β″-Alumina | Sodium to assess the voiding and dendritic behaviors of the sodium metal electrode at varying cycling parameters and operating conditions. By modifying the applied current density and fixing areal capacities at 0.5, 1.0, and 3 mAh cm^{-2} and utilizing a sodium reference electrode we demonstrate polarization on plate at high current densities. Modeling comparisons with exhaustion strips, unidirectional current application to oxidize the sodium metal electrode until a cutoff potential of 1 V, indicate extensive delamination of the sodium electrode from the solid electrolyte. There is less observed delamination at lower current densities as the cutoff voltage is reached at lower areal capacities. Further study of electrode thickness and operating pressure on critical current densities, the highest achieved current

density before failure to 1 V or shorting observed, and achievable capacities show limited benefit to increasing operating pressure beyond 2.0 MPa. We continue our investigation into interfacial behaviors through the assessment of hot pressing effects on argyrodite sulfide electrolytes with respect to morphology, ionic conductivity, and mechanical properties. We find that hot pressing at 150 °C improves ionic conduction without any reliance on external operating pressure with copper electrodes. Hot pressing resulted in smooth fused morphology distinct from the cold pressed (20 °C) samples with an higher modulus. Finally, our efforts in the development of an all solid-state battery database for laboratory scale single set of layer devices is discussed. We identified from the literature the core characteristics and performance metrics for a solid-state batteries and defined the ontology to capture the data for analysis. The ontology was tested and refined through the collection of fifty cells with the target of assessing the state of research, current achievements, gaps, and trends in the literature. The database now contains over 250 cells with plans for further uploads and refinements to the ontology.

MEASURING INTERFACE EFFECTS IN SOLID-STATE BATTERIES

by

Karl Larson

Dissertation submitted to the Faculty of the Graduate School of the

University of Maryland, College Park, in partial fulfillment

of the requirements for the degree of

Doctor of Philosophy

2025

Advisory Committee:

Associate Professor Paul Albertus, Chair
Associate Professor Taylor Woehl
Professor Yifei Mo
Assistant Professor Po-Yen Chen
Professor Eric Wachsman

Dedication

To the Lord, of whom I learn to appreciate even more through the study of His wondrous creation, the order and surpassing complexity of existence, and the spirit of thought and curiosity He has instilled in humanity displayed in my advisor and fellow students. Thank you for the opportunity, the blessings that are my fellow students, researchers, and my advisor.

To my wife, Meredith. Thank you for your love and support, patience, encouragement, and wisdom through the years. You have emboldened my heart and encouraged me to keep trying every day.

To my family, thank you for your encouragement and support through these years.

Acknowledgements

I would like to thank my advisor, Dr. Paul Albertus. He took in a student with no previous electrochemical experience and brought him through multiple publications and presentations, guiding me to greater understanding in the world of electrochemistry and independent research. More, he accommodated my erratic schedule that came with having children while providing thoughtful, compassionate advice and encouragement. I also thank all the colleagues in the lab and office over the years: Dr. Nathan Johnson who encouraged me to apply to the PhD program and gave support throughout it, Dr. Eric Carmona who gave advice on my projects, insights into electrochemistry, and encouragement throughout, Bhuvsmita Bhargava who I had the privilege to be in the same cohort and lab, Joshua Little, my friend whose banter and discussion about how to proceed helped me every week, Dr. Yueming Song, Dr. Caitlin Parke, Dr. Taeho Jung, Dr. Keith Duncan, Zixuan Wang, Taiwo Ogundipe, Michael McKee, Florencia Petracci, Michael Danner, Dr. Gibson Scisco, Dr. Evans Gritton, William Schubert, Adam Blickley, and Ryan Moore. Without this community I would never have been able to proceed, thank you all for your patience, insight, and conversations throughout the years. I would also like to thank George Jamaldinian, an undergraduate researcher who facilitated much of the experimental planning. I would like to thank our collaborators in the BIRD consortium, especially Dr. Yang Wang, Dr. David Zitoun, Dr. Alexander Kozen, Dr. Sang Bok Lee, Dr. Gary Rubloff. Finally, I would like to thank my committee members, Dr. Po-Yen Chen, Dr. Yifei Mo, Dr. Taylor Woehl, and Dr. Erich Wachsman. Thank you for sitting on my committee and offering insights and questions into this work.

This work was supported by the U.S.-Israel Energy Center program managed by the U.S.-Israel Binational Industrial Research and Development (BIRD) Foundation.

Table of Contents

Table of Figures

Chapter 2

List of Abbreviations

LLZO	$Li_{6.5}La_3Zr_{1.5}Ta_{0.5}O_{12}$
NBA	Na-β″-Al_2O_3
CCD	Critical Current Density [mA cm^{-2}]
ASR	Area Specific Resistance [Ohm cm^{-2}]
SE	Solid Electrolyte
LPS	Li_3PS_4
WE	Working Electrode
RE	Reference Electrode
CE	Counter Electrode
PEIS	Potentiostatic electrochemical impedance spectroscopy
GEIS	Galvanostatic electrochemical impedance spectroscopy
CDR	Current density ramp
I	Applied Current [mA]
i_o	Exchange Current Density [mA cm^{-2}]
$A_{Geometric}$	Area of the Fabricated Electrode [cm^2]
F	Faraday's Constant
α_c	Cathodic Charge Transfer Coefficient
α_a	Anodic Charge Transfer Coefficient
R	Ideal Gas Constant
T	Temperature
LPSCl	Li_6PS_5Cl

Chapter 1: Background

- Usual spiel about batteries being promising next generation technology for energy storage
- Description of the limitations in solid state batteries arising from solid-solid interfaces and the efforts to characterize and resolve them

Chapter 2: Reference Electrode Reveals Insights on Sodium Metal/Solid Electrolyte Interface Cycling and Voiding Behaviors at High Current Densities and Areal Capacities

Introduction

Distinct failure mechanisms of metal electrode / solid electrolyte interfaces include dendritic growths and void formation[1,2]. Both result from metal flux imbalances at the interface when (1) plating current becomes sufficiently large in localized regions to exceed the movement of metal away from the interface (dendrite) or (2) stripping current consumes metal faster than it can move back to the interface (voids)[3]. While dendritic shorts lead to the cell voltage dropping, sometimes to zero and sometimes to a non-zero value, void formation appears as cell area-specific resistance (ASR) increase. Voids may be partially replenished on the subsequent plate, but they are often observed to increase in number and size on each sequential strip[4]. A study of the Li/LLZO/Li system with impedance tests interspersed during strip at 0.1 mA cm^{-2} estimated a loss of 94% of the contact area due to voiding, without external mechanical stress[5]. Cycling and failure behavior at high areal capacities (i.e., >4 mAh/cm^2, to reflect current high-energy Li-ion cell loadings) is of particular interest as the cycling parameters strongly influence stripping and plating behaviors.

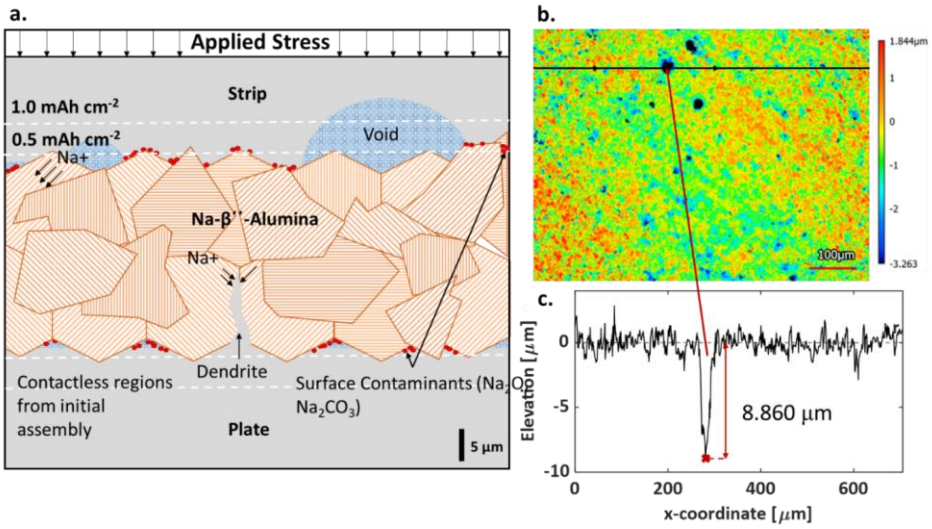

Figure 2.1 Current focusing influences for the Na/NBA interface. a. Schematic of an Na/NBA/Na cell. The schematic demonstrates phenomena that can lead to current restriction: surface geometry, surface contaminants, grain orientation and grain boundaries, and alkali metal mechanical properties. White lines of the grains represent the conduction planes whereas orange lines represent the spinel blocks of the NBA. b. Surface topology scan of the NBA disc surface used in our study. c. Plot of the surface elevation along the indicated black line in panel b.

At least four important factors influence interfacial metal flux imbalances affecting voiding behaviors, which we discuss in the following order:

1. Surface geometry
2. Surface contaminants
3. Grain orientation and grain boundaries
4. Alkali metal mechanical properties

These factors are depicted schematically in Figure 2.1. First, neither a solid electrolyte pellet nor a metal electrode foil are atomically smooth. When they are pressed together the metal and solid

electrolyte will not be in contact in some areas. It is necessary in some cases to apply pressures up to 40 MPa to approach the expected contact resistance of a surface in full contact[6,7]. EIS studies indicate stack pressure improves contact but close SEM back scattering indicates contactless regions even for low measured ASR[4,5,8–11]. Polishing the SE and using interlayers have been shown to alleviate the surface roughness effects by enhancing contact between Na/Li and the SE[12]. Second, surface contaminants such as alkali carbonates and hydroxide groups create resistive interfaces between the Na/Li metal and the SE. This is commonly reduced through heat treatments and polishing methods to achieve interfacial resistance as low as 1 Ω cm^2 [11–13]. A third set of factors that affect flux imbalances are grain orientation and ionic conduction pathways of the SE, as determined by grain and grain boundary properties. Grain boundaries at the interface may create ionic conductivity heterogeneities as those grain-grain interfaces exhibit different ionic conductivity as opposed to the bulk grain[14,15]. Further, 1D and 2D conductors exhibit grain orientation dependence for ionic conduction pathways, which can contribute to current focusing[16,17]. However, a systemic study of the influence of grain size and orientation on interface plating/stripping stability is lacking. And fourth, alkali metal properties influence flux imbalances at the anode-solid electrolyte interface. Sodium and lithium metal foils are typically used in solid-state battery cell research4,5,9,10,19–21. Sodium metal is soft, with an elastic modulus of 4.6 GPa at room temperature and yield stresses under compression of 0.16-0.24 MPa and 0.19-0.28 under tension [23]. Lithium metal possesses a larger 0.7-0.8 MPa yield strength under tension and an elastic modulus of 7.82 GPa [24,25]. While such low yield strength may be expected to indicate rapid alkali metal flow to the solid electrolyte surface after plastic deformation, it is not observed experimentally. Instead, deformation is dependent on the thickness of the metal foil at room temperature, with Li metal foils 100 microns thick showing little appreciable difference in

deformation at 1, 5, and 10 MPa while 700 micron thick Li metal foils have significant deformation at those same applied pressures24. Further, frictional and adhesive forces at the interface inhibit the metal flow, suggesting the surface morphology of a solid electrolyte may also affect metal deformation. Sodium metal adheres strongly to a clean oxide surface, resisting flow more than on smoother surfaces or surfaces with less adhesion22. As such, applied pressures from 1 to 5 MPa may be insufficient to ensure complete contact with a solid electrolyte at room temperature.

In addition to these four factors, cycling conditions including current density, areal capacity, temperature, etc. affect the flux imbalances. In the sodium metal system, 1.0 mAh cm^{-2} corresponds to a thickness of 8.84 microns, while the surface roughness of polished NBA surfaces can reach up to tens of microns. Hence, an areal capacity of 1 mAh cm^{-2} may not exceed the surface roughness of some interfaces. Indeed, it is known that increasing the per-cycle areal capacity during current density ramps (CDR) reduces the critical current density of a system[27]. Further, in reference 27 notable cell resistance rise was displayed well before the stated critical current density (CCD) for the 3 mAh cm^{-2} cell, indicating strong void behaviors well before defined failure at 0 V [27]. From consideration of these numerous factors affecting flux imbalances, insofar as a metric such as CCD can even be well defined, it is clear that it depends on many concurrent factors, including the cycling parameters.

We also note that much of the work in this field uses two-electrode, symmetric cell configurations (i.e., Metal/SE/Metal configurations, without a reference electrode). Three electrode systems are a known and well used method for cycling investigations in Li-ion research, [28–30] but we have identified less than a dozen papers on solid state three electrode cycling[4,20,31–38]. Two electrode system interpretations often presume cell polarization is only from the electrode undergoing stripping (where voids are expected), and the plating electrode acts as a stable pseudo-

reference electrode, but this is often not investigated carefully. Adding a reference electrode, albeit difficult to implement and not without its own limitations, can decouple the interface behaviors in symmetric cells. The powerful insights on the individual electrode interface behavior can help distinguish the mechanisms and influences of current focusing at the metal/SE interface during plating and stripping.

In this paper, we perform cycling under a fixed external mechanical load of 100N (2.6 MPa) with four types of cycling protocols. Three of those protocols are current density ramps at areal capacities of 0.5, 1.0, and 5.0 mAh cm^{-2}, and the fourth protocol is unidirectional stripping at the working electrode to determine the fraction of the initial metal foil removed prior to the voltage cutoff, again at a fixed 100N (2.6 MPa) load. For the current density ramps, 0.5 mAh cm^{-2} is chosen for cycling conditions that do not exceed the surface roughness of our NBA SE pellets, and to reflect a value commonly used in literature. 1.0 and 5.0 mAh cm^{-2} are chosen to reflect the plating and stripping depth within the pores of a 3D porous metal electrode and a 2D planar cell respectively[39]. We find a strong dependence of the cycling behavior on the areal capacity, emphasizing the importance of the cycling conditions on interfacial behaviors. We use a reference electrode to enable interpretation of the electrochemical behavior in the context of physical aspects of the stripping and plating reactions that occur at each Sodium metal / NBA interface. For the purposes of this paper, the electrode on the same face of the NBA as the RE is considered the working electrode and the electrode of interest. Our three-electrode system indicates much different behaviors between the low (0.5 mAh cm^{-2}) and high (5.0 mAhcm^{-2}) areal capacity tests during both stripping and plating. During plating at 5 mAh cm^{-2} and >3 mA cm^{-2}, we observe a time-varying interfacial potential at the plating electrode, the first in the literature to our knowledge, and potentially indicative of void formation on plating or another process. We

augment our experimental measurements with a model that relates the observed polarization with the amount of electrochemically active contact area. Our data indicates a strong relationship between the current density that can be sustained without dendrite or void formation and the areal capacity. Further, our data and model suggest that sustained stripping of dozens of hours may occur even with a modeled contact loss of >60%.

Methods

A picture of the assembled experimental platform is shown in Figure 2a, and the electrode arrangement is shown in Figure 2.2b.

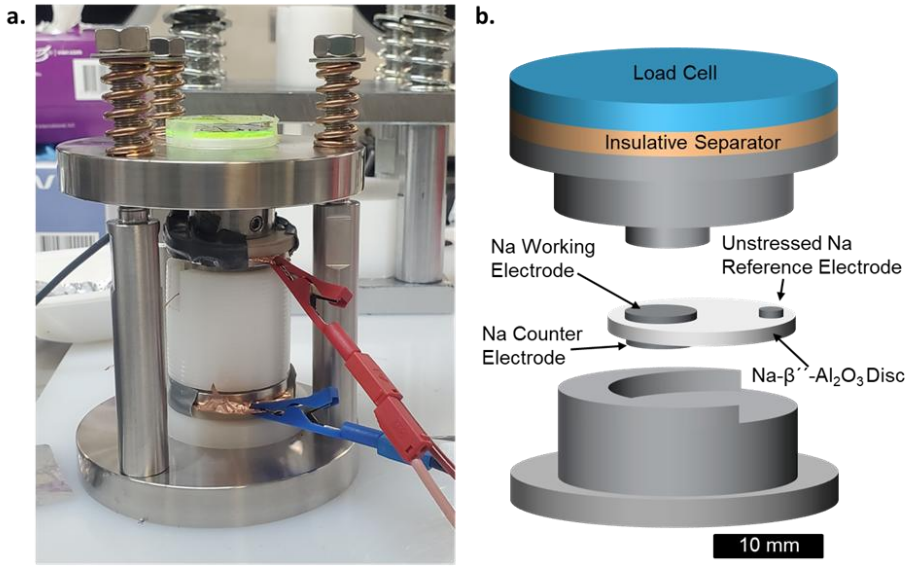

Figure 2.2 Experimental System a. Experimental platform configured in a two-electrode configuration for EIS testing. **b.** Schematic of the platform with arrangement of the three sodium electrodes on the NBA.

Solid Electrolyte preparation. SE discs composed of Na – β'–alumina (NBA) were purchased from Ionotec with dimensions of 20 mm in diameter and 1 mm in thickness. The discs were heat

treated to remove surface contaminants using a ramp of 4°C min^{-1} from room temperature to a hold at 850 °C for 2 hours in an MTI Muffler Furnace within an Ar-filled glovebox.

Na/NBA/Na Three Electrode Cell Assembly. Sodium foils were prepared from a sodium ingot purchased from United Nuclear. Oxidized layers were trimmed from the ingot and a piece cut from the ingot and laid onto clean aluminum foil. The foil was folded over the sodium metal and the entire piece cold rolled to the thicknesses of 300 or 500 microns. The results shown in this paper are all for 300 micron foils. The aluminum foil prevents the sodium metal from adhering to the cold rolling device. Foil thickness was measured using calipers and the measured thickness of the aluminum foil was subtracted to determine the sodium foil thickness. The aluminum foil was then peeled off of one side of the sodium and the exposed surface of the sodium was polished with a nylon brush. Electrodes were punched to 7 mm diameter discs with one side capped by aluminum foil. The sodium foils were pressed opposite each other onto the NBA disc 2 mm from the edge of the disc. Note that an area increase in the 300 micron foils during test was observed in some cases to ~8.5 mm in diameter, a 21% increase in diameter. Throughout this work we use the original diameter of 7 mm to for the area. The reference electrode was formed by wrapping a small (1 mm diameter) piece of polished sodium metal around the end of a copper wire. The sodium covered end of the wire was then pressed against the NBA disc and secured by copper tape. The disc with electrodes was then placed for 30 seconds on an ~ 80 °C hot plate to improve the contact between the sodium metal and the NBA SE; no pressure was applied during this warming step to avoid spreading of the Na electrode. Each side of the disc was heated in this way.

The cell was loaded into the inset of a custom machined bottom die with a custom alignment sleeve in place. The WE was aligned under the upper die protrusion for force

application. Both upper and lower die serve for force application and as electrical contacts. When assembled, the RE is the sole unstressed electrode. Alligator clips were attached to copper foils connected to the upper and lower die. Noise of 2-3 mV in magnitude in the potential response is noted in the data and is attributed through trial and error to the electrical processes of the glovebox.

Electrochemical Characterization and Cycling: Two electrode PEIS using a Biologic SP-300 was performed to characterize the resistance of the grain boundaries, bulk, and interface. The frequency range was from 7 MHz to 100 mHz.

The Biologic SP-300 was also used for galvanostatic cycling. Current Density Ramps (CDR) were designed with ten-minute rest steps between each half cycle, with 0.25 mA cm2 increments, for a current density range of 0.25 to 20 mA cm^{-2} (or until the cell showed shorting or the test voltage limit was reached due to resistance rise). Uni-directional stripping at the WE until the cell voltage limit was reached was performed at 0.3 and 1.2 mA cm^{-2} at 100 N (2.6 MPa) to test the limits of the achievable areal capacity from 300 micron thick foils. All electrochemical experiments and post-mortem pictures were done in argon chamber at room temperature under 100 N (2.6 MPa) applied force.

Modeling. We conducted simulations using the finite element analysis software COMSOL Multiphysics and the Secondary Current Distribution package. The working, counter, and reference electrodes were treated as Na metal. The solid electrolyte was treated as NBA and modeled as an isotropic material. We used the ionic conductivity reported by Ionotec, and provide this value and other parameters in Table 2.1. The exchange current density was estimated from our experiments, using the Butler-Volmer equation and assuming complete interfacial contact and the

as-fabricated interfacial area. The current distribution at the electrochemically active interfaces was solved using the Butler-Volmer equation. Ohm's law was solved in the electrolyte, as it is a single-ion conducting material that does not generate concentration gradients. To simulate contact loss resulting in the reduction of electrochemically active interface, a function was written in MATLAB that sets the exchange current density of the WE/Electrolyte interface to zero for a portion of the interface. The function allows the specification of the size of the regions where the exchange current density is zero (i.e. void width) and the percentage of the interface where the exchange current density is zero (i.e. number of voids).

Table 2.1. Modeling parameters for a temperature of 25°C.

Symbol	Parameter	Units	Value
i_o	Exchange Current Density	$mA \cdot cm^{-2}$	4
σ_{Na}	Sodium Electronic Conductivity	$S \cdot cm^{-1}$	$2.1 \cdot 10^{5}$
κ_{NBA}	Electrolyte Ionic Conductivity	$S \cdot cm^{-1}$	$2 \cdot 10^{-3}$

Results and Discussion

This results and discussion section will focus on the four main experiments done in this work, including (1) current density ramps with a fixed areal capacity of 0.5 mAh cm^{-2} per half cycle, (2) current density ramps with a fixed areal capacity of 1.0 mAh cm^{-2} per half cycle, (3) current density ramps with a fixed areal capacity of 5.0 mAh cm^{-2} per half cycle, and (4) uni-directional stripping at the working electrode of an as-built cell. In addition, there is (5) a section on modeling to provide a quantitative link between the amount of resistance rise on stripping and the interfacial contact area. We note that while the following figures show results from a single cell for each condition, we did at least three replicates for each cycling condition and chose a representative cell to present. The 0.5 and 1.0 mAh cm^{-2} conditions exhibited CCDs ranging from 10-12 and 7-12 mA cm^{-2} respectively. More importantly, the potential responses on half cycles remained consistent through all replicates.

Cycling behavior during a current density ramp at 0.5 and 1.0 mAh cm2 areal capacities

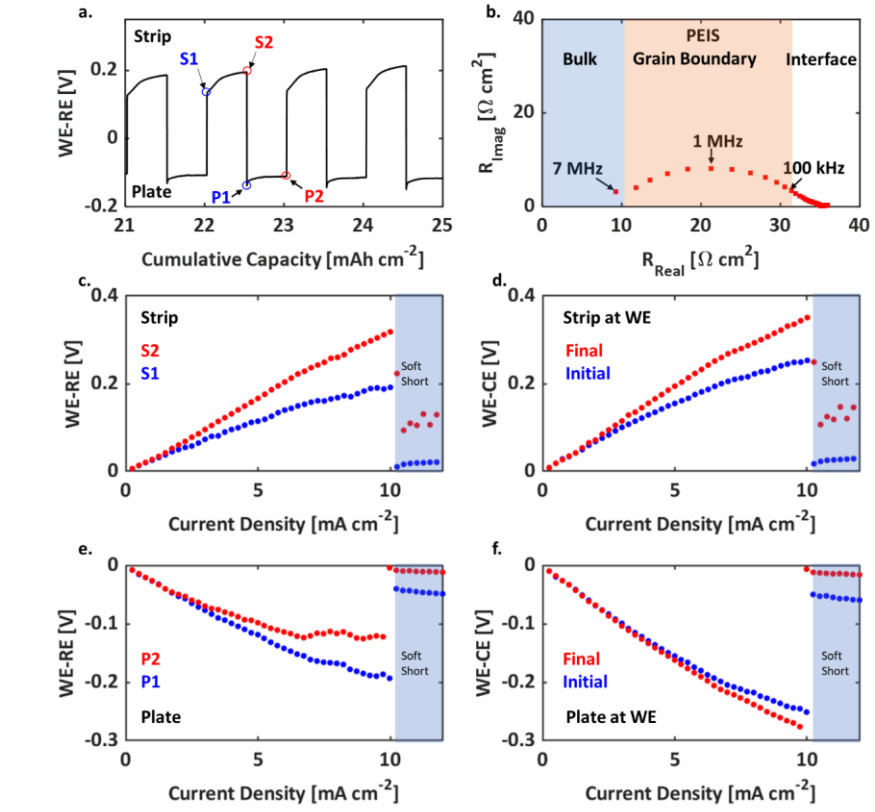

Figure 2.3 Cycling Data for 3-electrode system. 0.5 mAh cm^{-2} per half cycle, 25 C Na/NBA/Na **a.** Plot of Voltage against cumulative areal capacity for the WE compared to RE at 4.75 mA cm^{-2}. **b.** Pre-CDR PEIS of the assembled cell between WE and CE. **C.** Initial (S1 blue) and final (S2 red) voltage points on strip for each respective current density of the half cycle for the WE. Shaded region is data after a soft short is observed. **D.** Initial (blue) and final (red) voltage points for each respective current density of the half cycle in the two-electrode (WE-CE) on strip for the WE. **E.** Initial (S1 blue) and final (S2 red) voltage points on plate for each respective current density of the half cycle for the WE. Shaded region is data after a soft short is observed. **F.** Initial (blue) and final (red) voltage points for each respective current density for the half cycle in the two-electrode (WE-CE) on plate for the WE. Shaded region is data after a soft short is observed.

Commented [PA1]: Add what current density this is for.

Figure 2.3 provides results for a current density ramp at 0.5 mAh cm^{-2}, with specific points of interest (S1, S2, P1, and P2) noted in panel a. Panel b shows pre-cycling PEIS performed on the discs and indicated interfacial resistance on the order of ten Ohm cm^2 with the regions (e.g., bulk grain boundary, interface) assigned based on the literature[40,41]. The low interfacial ASR is attributed to the heat treatment performed on the NBA before cell assembly and is consistent with previous studies into the effect of heat treatment to improve interfacial resistance[13]. Warming the cell after applying electrodes is also known to enhance contact between metal and electrolyte and reduce interfacial resistance, but the low interfacial resistance is not assumed to be from "perfect", intimate contact. Fig. 2.3 panels c-f show a polarization vs. current density slope whose magnitude falls with rising current density (i.e., falling resistance with increasing current density). This is expected for Butler-Volmer kinetics. We interpret minimal deviation of S2 from S1 as the flux of Na^+ away from the interface not yet exceeding the flux of Na metal to the interface to create significant contact loss. The separation of S1 and S2 rises above ~2 mA cm^{-2}. As the current density increases beyond 2 mA cm^{-2}, the electrode experiences a resistive increase we attribute to contact loss over the course of the strip half cycle.

P1 and P2, as with S1 and S2, do not deviate significantly before ~ 2 mA cm^{-2}. Reflecting the higher resistive state at the end of the strip half cycle (S2), P1 increases in magnitude. As shown in panel a, once plating begins the resistance drops in the first 0.05 mAh cm^{-2} and we hypothesize the Na metal quickly grows from the edge of the voids inwards to reform the interface contact with the electrode. Fig 2.3 panels d and f show results for WE-CE, which is what most researchers measure. A comparison, for example, of panels e and f indicate that P2 and P1 (for WE-RE) separate more than Initial and Final (for WE-CE), which results from the increasing polarization during stripping offsetting the decreasing polarization during plating.

Moreover, on plating for the WE-RE data (panel e) the potential magnitude at the end of the half cycle (P2) is smaller than at the beginning (P1), while for WE-CE (panel f) the potential magnitude at the end of the half cycle is larger than at the beginning. This demonstrates that even at 0.5 mAh cm^{-2}, a reference electrode provides additional insights not reflected in data without a reference electrode.

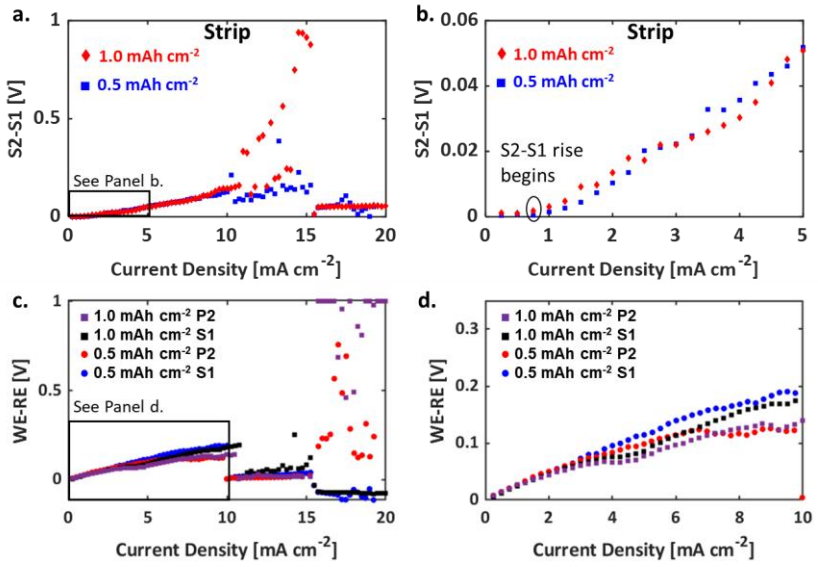

Figure 2.4 3-Electrode data for both 0.5 and 1.0 mAh cm^{-2}. A. The difference between the S1 and S2 WE-RE voltage per respective current density of the CDR, including shorted regions, for 0.5 (blue square) and 1.0 (red diamond) mAh cm^{-2}. **B.** The difference between the S1 and S2 per respective current density of the CDR for WE-RE, including shorted regions, for 0.5 (blue square) and 1.0 (red diamond) mAh cm^{-2} for the lower (0.25-5 mA cm^{-2}) current densities. **C.** P2 and S1 for the same current density cycle for 0.5 (circle data point) and 1.0 mAh cm^{-2} (square data point). **D.** The same data from **c.** plotted from 0.25-10 mA cm^{-2}.

In Figure 2.4 we retain some of the CDR results for 0.5 mAh cm^{-2} from Fig 2.3, but now add results for 1 mAh cm^{-2}. Panels a and b show the difference between S1 and S2 vs. current

density. This value represents the polarization rise during the stripping half cycle. The cells experience soft shorting at 10.75 and 10.25 mA cm^{-2} for the 0.5 and 1.0 mAh cm^{-2} cells, respectively. For both areal capacities, S2-S1 begins to rise at about 1 mA cm^{-2}, and continues to rise in a similar way until failure. As demonstrated in Figure 2.1, the average surface roughness of our NBA discs is greater than that of the 0.5 mAh cm^{-2} depth of strip (4.42 microns) with some features of the SE exceeding the depth of the 1.0 mAh cm^{-2} (8.82 microns). As the depth of plate/strip of neither 0.5 nor 1.0 mAh cm^{-2} clearly exceed the surface roughness, it is expected that their polarization rises are similar.

One notable behavior that the three-electrode data reveal is the difference between P2 and S1 for the same current density, as shown in Figure 4c-d. Because the physical state of the interface at P2 and S1 should be very similar (one follows the other in the cycling protocol), we expected P2 and S1 to match for the same current density. However, beginning at ~ 3.75 mA cm^{-2}, a disparity between the values begins, and S1 increases at a greater rate than P2. Several factors may influence this behavior. Firstly, the data shown is for the WE-RE with the order of operations strip-rest-plate. Hence, there is a 10 min rest between P2 and S1, and interface relaxation (e.g., Na metal flow) could occur. Another possibility is that we collected data at fixed one second intervals, which may not capture rapid (<1 second) changes in interface potential associated with a rapidly changing presence of Na metal at the interface. Thus, the reference electrode reveals further behaviors not displayed in a two electrode system.

Cycling behavior during a current density ramp at 5 mAh cm^{-2} areal capacity

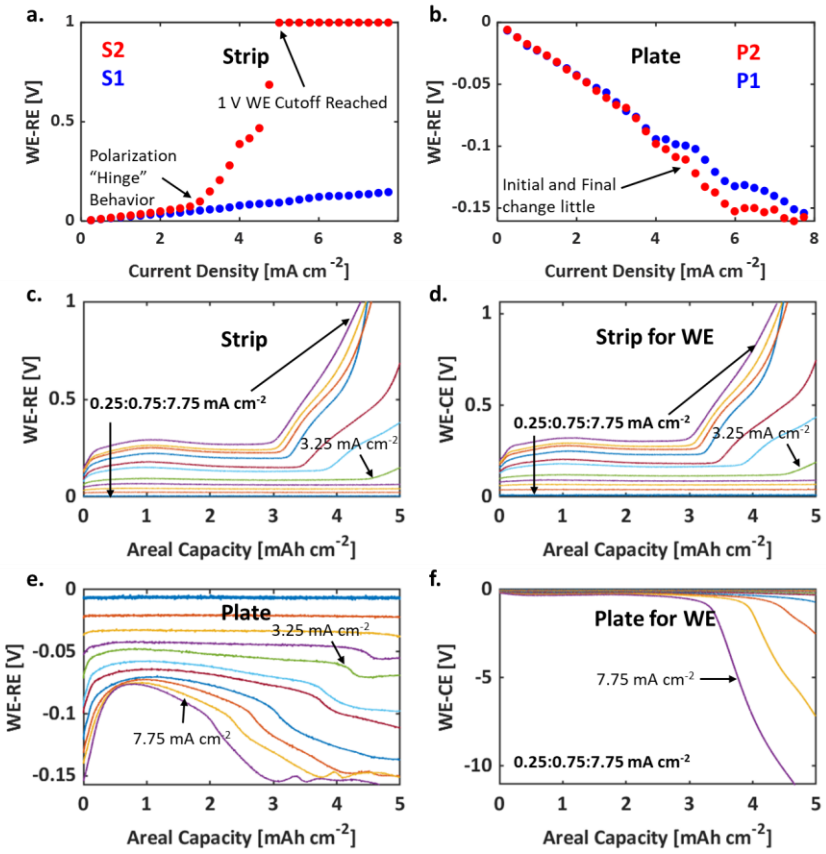

Figure 2.5 Cycling behavior at 5 mAh cm^{-2}. 25 C, Na/NBA/Na **a.** Initial (S1 blue) and final (S2 red) voltage points against the respective current density for the half cycle on strip for the WE. **b.** Initial (P1 blue) and final (P2 red) voltage points against the respective current density for the half cycle on plate for the WE. Note the distinct difference in polarization behavior as compared to the lower current density CDR in Figure 4. **c.** Voltage response of the WE against the RE plotted against the corresponding areal capacity in mAh cm^{-2} for the half cycle on strip. **d.** Voltage response of the WE against the CE on strip for the WE plotted against the corresponding areal capacity in mAh cm^{-2}. **e.** Voltage response of the WE against the RE plotted against the corresponding areal capacity in mAh cm^{-2} for the half cycle on. **f.** Voltage response of the WE against the CE on plate for the WE plotted against the corresponding areal capacity in mAh cm^{-2}.

At the 0.5 and 1 mAh cm^{-2} areal capacities shown above, the depth of strip/plate was under 10 microns. We proceeded to assess the cycling response of these symmetric cells at 5 mAh cm^{-2}, or ~ 42 microns of Na depth, as this is considered of greater relevance for commercial applications. Figure 2.5 shows results for a 5 mAh cm^{-2} CDR test, and significantly different behaviors for both plating and stripping are observed compared with 0.5 and 1 mAh cm^{-2} testing. As shown in panel 2.5a, S2 has two different behaviors, differing from the steady increase with current density shown by S1. In the first region from 0.25-2.75 mA cm^{-2} S2 exhibits a small deviation from S1 and a nearly linear rise. At 3 mA cm^{-2} a hinge in the response is observed with S2 rising quickly to reach the cutoff voltage. Panel 2.5b displays no separation of P2 from P1 in the same current density range unlike the separation observed in the 0.5 and 1.0 mAh cm^{-2} CDRs. A two-stage behavior on strip is shown in Panel 2.5c. Upon the start of the strip the potential jumps quickly before settling on a nearly flat voltage "plateau". After 3 mA cm^{-2}, a stage of polarization rise occurs. The inflection point for this potential rise decreases with increasing current density. The WE-RE data in panel 2.5c is similar in appearance to that of the WE-CE data in 5d.

Next we turn to panels 2.5e and 2.5f, which shows results for plating at the WE. Just as the stripping behavior experiences a two region polarization, so too does the plating. At <~0.5 mAh cm-2, the voltage magnitude falls, and then it begins to increase (at least for >3 mA cm-2), which we interpret as dynamic interfacial recovery following the previous strip. It is also notable that the voltage at the end of plate is similar to that at the start. The two-region polarization appears on both plate and strip at 3 mA cm^{-2}. This may indicate that stable cycling up to 3 mA cm^{-2} is possible for this system even at 5 mAh cm^{-2} or 42 micron depth of strip and plate. However, further investigation of these hinge behaviors is necessary with evaluation at different

applied forces and other cycling conditions. We also note that the two-region polarization behavior during plating is masked in the WE-CE data because the stripping electrode dominates the response. To the best of our knowledge this is the first time a resistive mechanism during plate of this type has appeared experimentally, and again results from our use of a reference electrode and also our exploration of high current densities and areal capacities.

What may account for the changing WE-RE polarization during plating at >3 mA cm^{-2} at the electrode undergoing plating? One possibility is void formation on plating, as suggested in a recent modeling work[42]. Another possibility is that the void formation on the stripping electrode leads to current focusing on the plating electrode that increases resistance. In other words, if current is confined to a small number of points on the stripping electrode, that will also reduce the area for plating because the current does not fully spread. This behavior would depend on the separator thickness and other factors that govern secondary current distributions.

Working electrode behavior during a uni-directional current stripping experiment

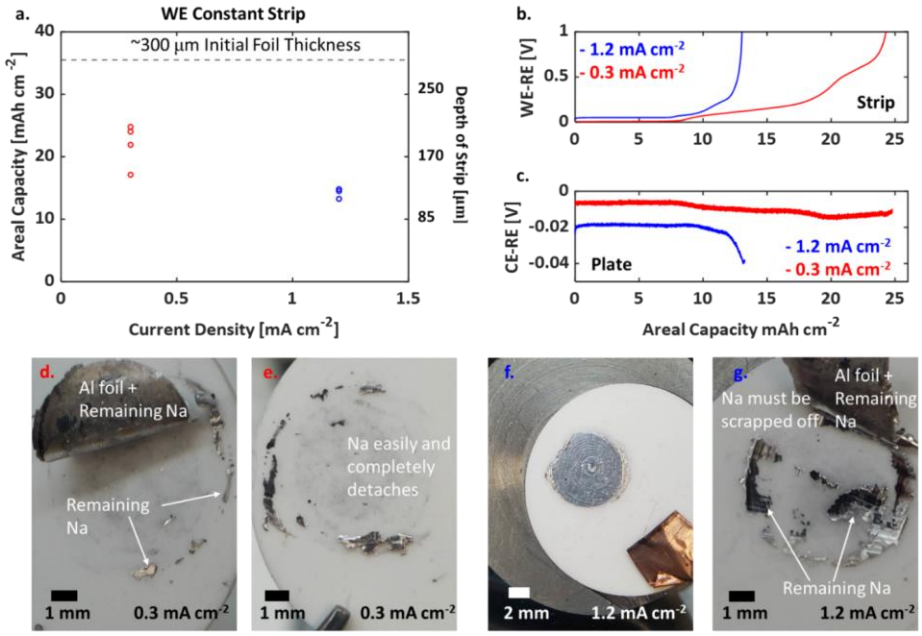

Figure 2.6 Unidirectional Cycling Data with Representative images of post strip cells. a. Plot of achieved areal capacity from one constant strip to exhaustion, defined by reaching 5V cutoff WE-RE, against the corresponding stripping current density. The dashed line represents the total initial areal capacity of the sodium foil. **b.** Potential vs areal capacity of the WE-RE for a 0.3 and 1.2 mA cm^{-2}. **c.** Plot of the potential vs areal capacity of the CE-RE for a 0.3 and 1.2 mA cm^{-2}. **d-e.** Post cycling images of the working electrode after constant strip of 0.3 mA cm^{-2}. Note the lack of metallic Na in the center of the electrode. **f-g.** Post cycling images of the working electrode after constant strip of 1.2 mA cm^{-2}. Unlike the 0.3 mA cm^{-2} examples, there is much more metallic sodium still in contact with the NBA that could not be removed with razor blade. In d., e., and g. the sodium surface is not black but appears such based on the lighting. The actual appearance of the remaining sodium was metallic gray.

While Figures 2.3 to 2.5 all show cycling results, in Figure 2.6 we show results for unidirectional stripping at the WE interface, such that the effects on the interface from previous cycles are absent. This test also allows us to estimate the fraction of the Na foil that can be passed before failure in the form of dendrite formation or ASR rise. As shown in Figure 2.6a, the

areal capacity achieved prior to the resistance rising and a cutoff potential being reached is well below that available in the foil. At the lower current density (0.3 mA cm^{-2}) the strip achieves a higher areal capacity than the higher current density (1.2 mA cm^{-2}). However, the 0.3 mA cm-2 test reaches at most ~25 mAh cm^{-2}, ~10 mAh cm^{-2} short of the total initial capacity with other replicates further below this. The higher current density (1.2 mA cm^{-2}) showed increased sample-to-sample consistency and a lower areal capacity. Of particular note is the 0.3 mA cm^{-2} stripping takes place even with >100 mV of polarization for tens of hours before the final rise to the voltage cutoff is reached. In other words, rather than a sharp "knee" in which voids form and the resistance quickly rises to the cutoff, the interface demonstrates substantial (>100 mV) polarization for an extended (tens of hours) time.

Post-mortem optical assessment of several cells shown in Figure 2.6 displayed clear differences between the 0.3 mA cm^{-2} and 1.2 mA cm^{-2} samples. At 0.3 mA cm^{-2}, the tests spanned 3 to 4 days, and optical images of the working electrode showed very little physical contact with the remaining foil at the end of the test. The foils readily peeled from the surface of the NBA pellet with little Na metal residue to indicate strong contact at the interface. All 0.3 mA cm^{-2} samples had little physical adhesion between the remaining sodium metal and the NBA surface as shown in Figure 2.6d and 2.6e. The 1.2 mA cm^{-2} samples in Figure 2.6f and 2.6g, conversely, had large sections of the sodium still in strong contact with the NBA to the point that it could not be removed with a razor blade. This indicates a limit to the achievable areal capacity at these conditions based on the current density applied. Future work will focus on elucidating which of the four identified influences on current focusing most affect these results.

Figure 2.6c. presents the voltage evolution at the CE where plating is taking place, and as seen in Figure 5, shows a rise in the potential of up to about 20 mV for 1.3 $mAcm^{-2}$. The 0.3 mA

cm^{-2} plating potential changes little even as the stripping electrode undergoes a large polarization increase. While the polarization changes at the plating electrode are small compared to those at the stripping electrode, we again point out that these changes are neither well identified nor accounted for in the literature. Whether this indicates that current restriction at the WE undergoing stripping is affecting that at the CE during plating is subject to future research. There is a clear difference between the polarization changes during plating for the 0.3 mA cm^{-2} and 1.2 mA cm^{-2} tests, indicating a rate dependence.

Model to relate interfacial polarization with contact area

To establish a quantitative link between the voltage rise (>1 V in some cases) and the corresponding electrochemical contact area, we constructed a model of a Na/NBA interface, including the placement of a RE to match our experimental setup. The model involves solving the secondary current distribution with Ohm's law in the electrolyte ($\kappa = 2\ mS\ cm^{-1}$) and the Butler-Volmer equation at the interface, with electrochemically active area having $i_0 = 4\ mA\ cm^{-2}$and inactive area having $i_0 = 0\ mA\ cm^{-2}$). Figure 7 shows the modeling domain and a representative case. Figure 2.7a demonstrates the resultant potential and the current distribution when using 10 µm voids that cover 50% of the interface and an applied current density of 1 mA·cm^{-2}. Regions where the interface is electrochemically active have a fixed value of the exchange current density 4 mA cm^{-2}. Figure 2.7b shows the current distribution at the WE/NBA interface for the same conditions. The reduction in electrochemically active interface causes a number of regions where the local current density drops to 0 mA cm^{-2}, which in turn increases the current density at active regions, with local current densities approaching 6 mA cm^{-2}.

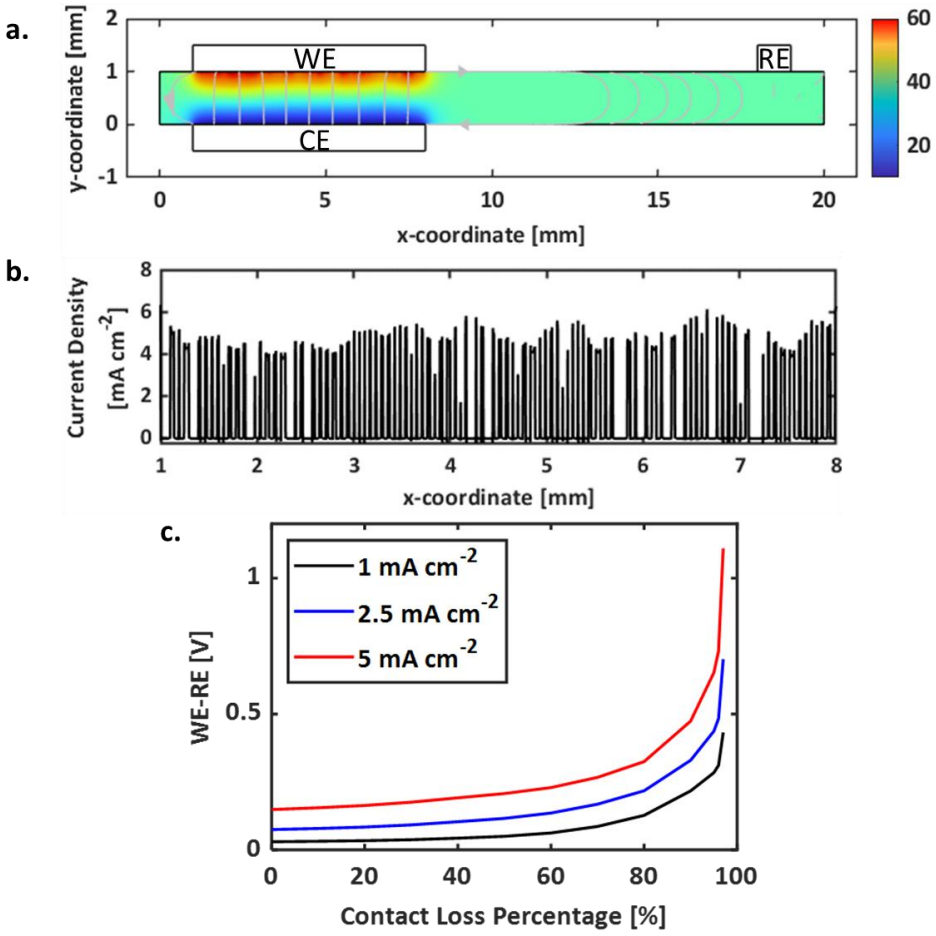

Figure 2.7 Two Dimensional model of the three electrode system. a. Potential surface plot and current distribution for an applied current of 1 mA cm^{-2}. 10 µm regions were used and 50% of the WE interface was set to inactive to simulate contact loss. **b.** Plot of the current distribution at the WE/NBA interface. **c.** Potential of WE vs. RE. against the percentage of electrochemically inactive interface (i.e. exchange current density is zero) for the current densities of 1, 2.5, and 5 mA cm^{-2} (black, blue, and red respectively).

Figure 2.7c demonstrates the polarization rise (WE-RE) as a function of the contact loss for several values of applied current density. For each case, the polarization increases monotonically, with more substantial polarization occurring beyond 80% contact loss. The modeling results presented in Figure 2.7c can be compared to Figure 2.5c as an estimate of the contact loss at various capacities stripped. The model indicates that for large polarizations, electrochemically active contact loss exceeding 90% is required. Note that if during the initial cell build there is inactive interface, that is not included.

This model has several limitations. Voids are assumed to be of uniform size, whereas there is likely a distribution of void sizes as well as increasing void size as stripping continues. The model is stationary, thus the dynamics of void formation and growth are not accounted for. NBA is treated as an isotropic material despite the fact that it is a polycrystalline material; therefore the effect of grain boundaries and grain orientation is neglected. The electrochemically active interfaces are treated as homogenous and impurity-free with no spatial variation in interfacial resistance or exchange current density.

Conclusions

We carried out cycling of a symmetric Na metal / NBA / Na metal cell with a Na metal reference electrode. In current density ramps at areal capacities of 0.5 and 1.0 mAh cm2, we observed cell shorting at ~10 mA cm^{-2}, however at an areal capacity of 5.0 mAh cm^{-2} we observed resistance rise to a cutoff potential rather than cell shorting. This is further evidence of how the cycling protocol, including both areal capacity and current density, strongly influence the cycling results, including even the mode of failure (e.g., dendrites vs. voids). Our reference electrode data shows that for the 0.5, 1.0, and 5.0 mAh cm^{-2} areal capacities, up to about 3 mA cm^{-2} the plating electrode demonstrates stable polarization and may be reasonably used as a

pseudo-reference electrode. However, at higher current densities, at any of these areal capacities, the reference electrode reveals significant time-varying interfacial polarization (with a magnitude of 10s of mV) at the plating electrode that is not easily identified with a two-electrode cell. The time-varying interfacial polarization at the plating electrode has not been previously observed and may indicate void formation on plating, the current distribution at the stripping electrode affecting the plating electrode polarization, or another process[42]. At the stripping electrode during current density ramps, our reference electrode data reveals that interfacial polarization rise during a stripping half cycle begins at 1 to 3 mA cm^{-2}, and for the 5 mAh cm^{-2} capacity at current densities over 5 mA cm^{-2} can grow to and exceed 100s of mV. The use of a reference electrode provides the quantitative separation of the time-varying interface polarizations that is not possible in a two-electrode cell.

Commented [PA2]: Cite Eric's paper again here.

In addition to cycling tests with fixed areal capacity and a ramp of the current density, we also carried out unidirectional stripping experiments (i.e., without cycling) at 0.3 and 1.2 mA cm^{-2} until cell failure due to voltage rise. Prior to the voltage cutoff, even at the low current density (0.3 mA cm^{-2}), ~30% of the initial Na foil cannot be stripped, and at 1.2 mA cm^{-2} about 60% cannot be stripped. Our 3-electrode cell shows that the voltage rise that drives cell failure is at the stripping electrode, as expected, but we again observe time-varying polarization at the plating electrode at the 10s of mV scale. Our data also directly shows that at 1.2 mA cm^{-2} hours of cell operation occurs with stripping electrode polarization at 100s of mV, and at 0.3 mA cm^{-2} tens of hours of operation with stripping electrode polarization at 100s of mV occurs. These observations provide direct quantitative insights on Na flux at a stripping electrode at high interfacial polarization conditions.

Finally, we developed an interfacial contact model to quantify the expected relationship between interfacial polarization and interfacial contact in our three-electrode cell. This model shows that an interfacial polarization of 100s of mV (as observed in several of our experiments) indicates >80% loss of the initial electrochemically active contact area. This substantial loss of electrochemically active contact poses important questions for the overall contact mechanics at the Na metal/NBA interface, and in particular the extent of the electrochemically inactive mechanical contact, and how the electrochemically active and inactive contact areas interact. We expect that the expanded use of a reference electrode in cells with metal/solid electrolyte interfaces, the careful design of cycling protocols, and additional interfacial modeling work, will further our understanding of the processes and quantitative limits of both metal electrode plating and stripping. We continue our analysis by addressing the operating pressures, surface roughness, and foil electrode thickness in the next chapter.

Chapter 3: Assessing Pressure and Electrode Foil Thickness on Voiding Behaviors in All-Solid-State Batteries

Introduction

Combating void initiation and growth requires methods that do not impede the electrochemical processes while minimizing the manufacturing and energy density costs. Efforts to mitigate voiding include 3-D structures, alloying the alkali metal, temperature and pressure.[43–46] Of these, pressure does not require any additional material within the cell to be added, preserving the energy density advantage of the metal anode without requiring high temperatures to operate. Pressure is beneficial in promoting stable cycling and increasing critical current density (CCD)

and achievable capacity from metal anodes.[46–48] The improved performance is attributed to increased contact area between the two solid interfaces of the alkali metal and the solid electrolyte by enhanced alkali metal flow to the interface.[49,50]

Exploring the limitations of pressure is of interest, especially at low operating stack pressures. High operating pressures induce mechanical failures of the solid electrolyte and promote dendrite formation at the interface.[50,51] As such, it is important to pursue understanding of the metal anode at lower operating pressures. Recent studies have studied the lithium behavior against various solid electrolytes with overall less focus on the sodium metal anode.[9,10,38,52–59] Here we focus our efforts again on the solid sodium metal anode. Using the same experimental configuration used in Chapter 2, we assess the effect of applied operating pressure on the polarization behavior of the Na | NBA system. Utilizing varying foil thicknesses, we show the system has a linear dependence on pressure for CCD between 0.5 and 5 MPa of applied stack pressure. Achievable capacity per pressure conditions is assessed with exhaustion strips as utilized previously and the overall overpotential during the strip recorded.

Methods

Sodium β″ Alumina solid electrolyte pellets of 20 mm diameter and 1 mm thickness were purchased from Ionotec. The discs were heat treated to remove surface contaminants using a ramp of 4°C min^{-1} from room temperature to a hold at 850 °C for 2 hours in an MTI Muffler Furnace within an Ar-filled glovebox as in done in our previous work.[60] For polishing, alumina particles suspended in isopropanol with progression of solutions from 500 nm to 0.5 nm were used with polishing cloths purchased from MSE Supplies to polish the surfaces of the pellets. The pellets were then rinsed in isopropanol and dried in the furnace at the above heating regime.

Sodium foil of 150 μm was purchased from MSE Supplies. The plastic backings were stripped from it and the foil polished using nylon lab brush and affixed to aluminum current collectors. 7 mm diameter electrodes were punched out and placed opposite to each other on either side of the NBA pellets 2 mm offset from the edge of the pellets. The pellet with CE and WE was warmed on a hot plate at roughly 70 °C for 5 minutes on either side before a RE was fixed onto the pellet. The RE was manufactured as in our previous work.[60]

Cycling was carried out using a Biologic SP-300. PEIS measurements were performed before and after CDR and exhaustion strips at 10 mV perturbation potential from 7 MHz to 100 mHz at a sampling rate of 6 points per decade. CDR and exhaustion strip follow our previous methods with an exhaustion strip current density of 0.3 mA cm^{-2} calculated off of the nominal electrode area. Pressure was maintained using a load frame with custom split cells to hold the cells with the WE and CE electrodes centered. Pressure was monitored by a U-93 load cell with a ClipX data amplifier.

Results and Discussion

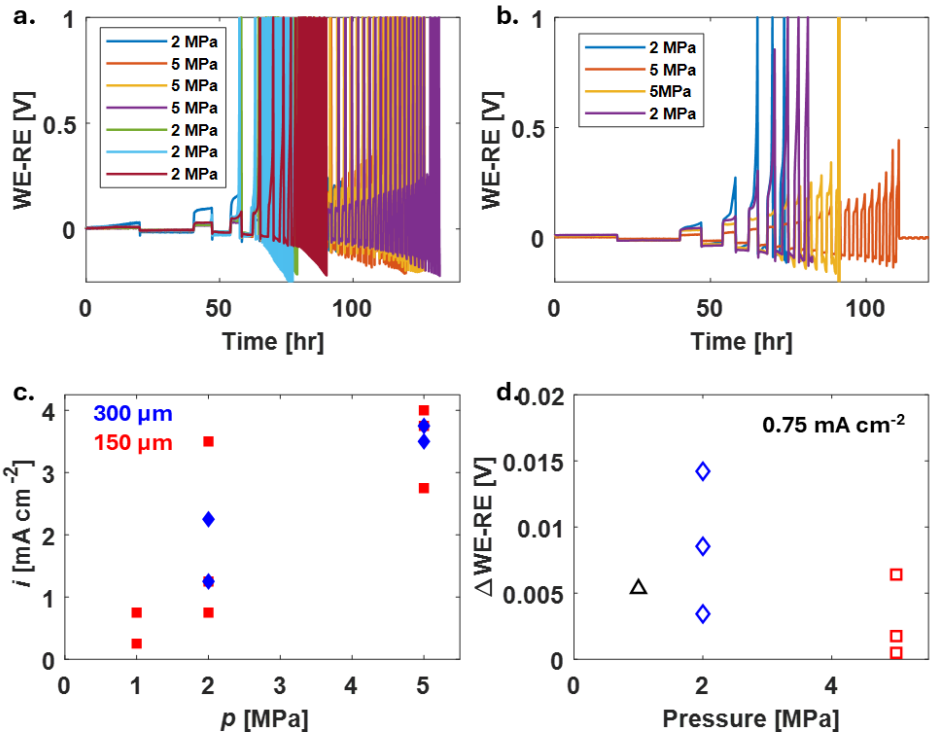

Figure 3.1 a. Plot of CDR profiles for 150 micron thick Na foils at different operating pressures (0.5 MPa not shown). **b.** Plot of CDR profiles for 300 micron thick Na foils at 2 and 5 MPa operating pressures. **c.** Plot of the critical current density for the 150 and 300 micron thick foils against operating pressures. **d.** plot of the overpotential from the 0.75 mA cm^{-2} strips of the CDRs calculated by subtracting the initial potential measured from the steady state potential of each curve.

Figure 3.1a-b shows the result of the CDR cycling of the 150 (a) and 300 (b) micron foil electrodes at varying operating conditions at 5 mAh cm^{-2} per half cycle. Consistent with Chapter 2 results of our previous work, the main mechanism of failure was catastrophic polarization to

the 1 V cutoff. Per our previous report, this is associated with delamination of the working electrode in extreme voiding at the interface. This can approach >90% contact loss between the sodium metal and the NBA even at the greater operating pressure of 5 MPa. This voiding is delayed at higher stack pressures but shows in both 300 and 150 micron cells. Indeed, Figure 3.1c shows the achieved highest current density until failure at 1 V is linearly dependent on the operating pressure and in all but one case is voiding the main mechanism. Moreover, the thickness of the electrode does not provide higher achievable current density in this study (Figure 3.1c), indicating that the stack pressure and areal capacity are more determinative of the operating stability. We attempt to assess how the increasing pressure improves achievable current density in Figure 3.1d. Here we compare the overpotential, represented by the absolute difference between initial potential measured by the galvanostat upon first current application on the 0.75 mA cm^{-2} oxidation (strip) and the average value of the plateau observed in the stripping profile (so called “steady state”). Though widely varying in response, it appears there is a small trend of overpotential decreasing with increasing pressure. This could be a result of increasing operating pressure reducing the number of nucleating voids through enhanced sodium metal deformation and pressure induced creep to the interface.

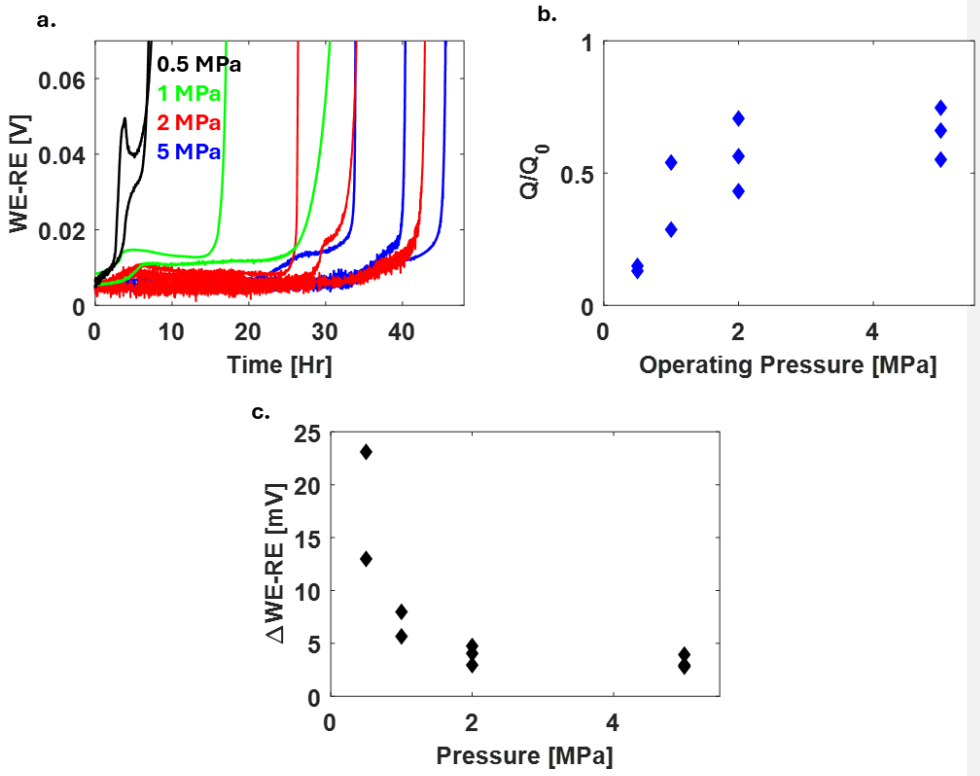

Figure 3.2 **a.** Plot of the exhaustion strips for the 150 micron thick sodium foils at the different operating pressures of 0.5 (black), 1 (green), 2 (red), and 5 MPa (blue). **b.** Plot of the achieved capacities (Q) normalized to the loaded capacity (Q_0) of the 150 micron thick foil (7.14 mAh cm^{-2}). **c.** Plot of the average potential from initial until 0.50 mV of each exhaustion strip to represent the respective overpotential of stripping at each pressure.

To further assess the impact of operating pressure on the performance of all solid state metal anodes against solid electrolytes, we performed exhaustion strips at 0.3 mA cm^{-2} at varying operating pressure. For this experiment we used only the 150 micron foils. Each cell was fabricated at 5 MPa and held there for one hour before being lowered to the desired operating pressure as needed. Figure 3.2a displays the stripping profiles of the cells at each operating pressure condition. For pressures 1 MPa and greater, the profile is consistent with a small initial

polarization in the first 0.15-0.20 mAh cm^{-2} before plateauing until a final sharp polarization indicative of large voiding at the interface. In the 0.5 MPa case a sharp polarization is observed far earlier in the half cycle with small shoulders indicating some possible short lived recovery before another rise reaching the 1 V cutoff. In both cases the achieved capacity was much reduced compared to the higher stack pressures.

Figure 3.2b shows the ratio of achieved capacity at each operating pressure against the loaded capacity of the 150 micron foil. We observe the achieved capacity has a logarithmic behavior for the operating pressures used in this study. The greatest dependency on operating pressure is observed in the low pressure regime with a quadrupling of the achieved capacity as the operating pressure increases from 0.5 MPa to 2 MPa. However, this trend appears to change after 2 MPa, with little notable improvement in achieved capacity at the 5 MPa case (the upper pressure limit of our study). This pattern is reflected in the overpotential of the exhaustion strips as shown in Figure 3.2c. Here the potential of the system, average of all measured values up to a measurement of 50 mV, decreases considerably from the 0.5 MPa to 2 MPa strips before leveling off. Of interest is that all pressures used here lie above the measured yield strength of sodium metal. As the metal behaves in a non-Newtonian manner.[61] As the average potential changes little between the 2 MPa and 5 MPa case, we theorize the operating pressure has a local limit to effectiveness. It is possible that foils <100 microns would exhibit stiffer behavior and play a larger role in voiding and dendrite behaviors leading to less achievable capacity.

Conclusion

We continued characterizing the failure mechanism of sodium metal against sodium β″ alumina at high areal capacity with reference electrode. Here we vary the operating pressure and foil thickness to discern the dependency of the critical current density on either. We observe that the

critical current density shows no discernable variance between the 150 micron and the 300 micron electrode sodium foils, indicating that the thickness of the foils involved does not impact operation at these conditions and for these thicknesses. Pressure reduced the overpotential development associated with voiding until higher current densities. Further assessment of achievable capacity at 0.3 mA cm^{-2} shows a strong pressure dependency from 0.5 to 2 MPa with little change beyond 2 MPa to 5 MPa. Of note is that the achievable capacity reaches on average 65% of the loaded capacity at 5 MPa. This is roughly the same amount as the 300 micron foils at the same current density at 2.6 MPa from our previous work. Thus the achievable capacity at pressures greater than 2 MPa may more be a function of aspect ratio than the operating pressure itself. We will continue to explore the effects of polishing and chemical interlayers on the achievable capacity to better understand what influences dominate at the alkali metal and solid electrolyte interface.

Chapter 4: Hot pressing argyrodite solid electrolyte powders results in >2 mS cm-1 ionic conductivity at 20°C and <1 MPa operating pressure

Introduction

Sulfide solid electrolytes are promising for all solid-state lithium batteries.[62,63] They possess relatively high ionic conductivity (10^{-3} – 10^{-2} S cm^{-1} at 25 °C) and their synthesis and processing compare favorably to oxide solid electrolytes.[64,65] Of the crystalline sulfide compositions, argyrodite-type may have lower manufacturing costs than $Li_{10}GeP_2S_{12}$ (LGPS) while maintaining lower synthesis temperatures than oxides.[66–68] Synthesis can occur via manual grinding solid-state reactions, wet chemical reactions, and high speed mechanical ball milling and requires few steps to achieve the final composition.[63,67,69] The formation of pellets from

argyrodite powders typically involves room temperature compaction at pressures of 100s of MPa, and operation at 10s to 100s of MPa.[70–73] In contrast, oxide solid electrolytes like LLZO garnet typically require high temperature (often >~1000 °C) calcination and sintering steps to form pellets, with some sintering steps including applied pressure.[74–76] Unfortunately, the advantage for the sulfides of low-temperature compaction are balanced by the reliance on the aforementioned large fabrication and operation pressures to achieve competitive ionic conductivities and cycling results.[51,59,77,78] Several studies have shown a clear correlation between fabrication pressure and pellet density, with higher density generally resulting in higher ionic conductivity.[79] Pellet porosity and microscopic gaps between particles are identified as limiting ionic transport, with operation pressure reducing these limitations. Because the cost-effective operating pressure limit for a cell in an electric vehicle battery pack is ~1 MPa, the required performance metrics (e.g., ionic conductivity), need to be achieved near or below this pressure.[80]

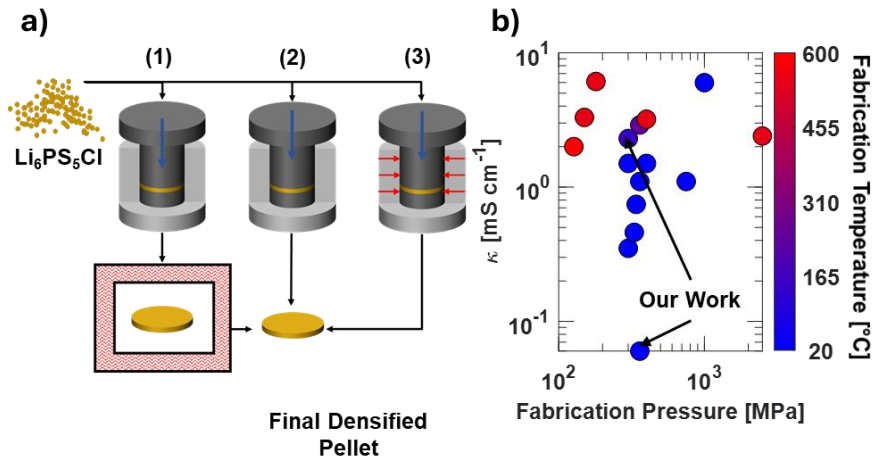

Condition	(1)	(2)	(3)
Pressure	30 MPa – 3 GPa	30 MPa – 3 GPa	300 MPa
Temperature	150-550 °C	20-25 °C	150 °C

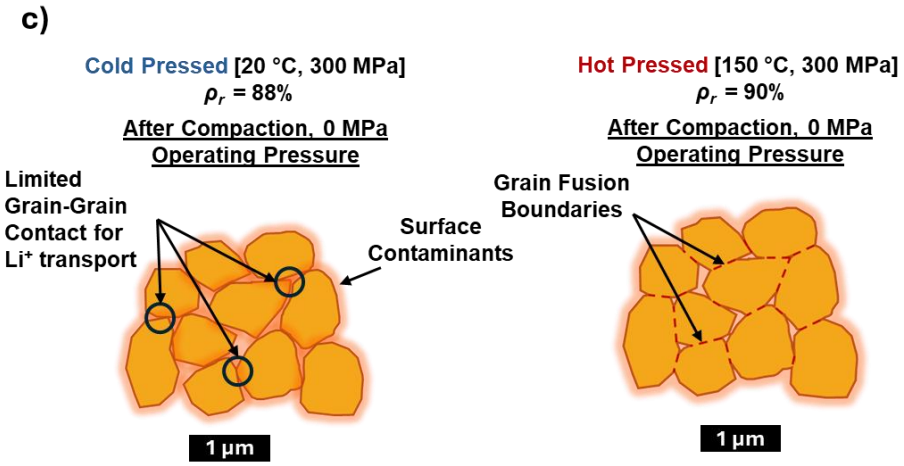

Figure 4.1 a. a schematic of different argyrodite compaction and compaction methods with (1) representing the typical high-pressure compaction at TFabrication = 20 °C (i.e. "cold" pressing) followed by pressure-free sintering, (2) representing typical "cold" pressing, and (3) representing the approach in this work with a single compaction

step with both pressure and elevated (i.e. "hot" pressing). **b.** a plot of literature results of ionic conductivities and their associated fabrication temperature and pressure.22–27,28–34 Here, the fabrication temperature shown is the highest temperature used for in either the sintering or pressing steps. **c.** Schematic of our proposed mechanism for the differences in grain morphology, ionic conductivity, and mechanical properties for pressing at 20°C ("cold pressing") vs. 150 °C ("hot pressing"). Potential surface contaminants, either from unreacted precursors or moisture degradation products, are represented by the shading around the grains.

Typically, efforts for improving ionic conductivity and cycling focus on increasing pellet density and improving grain-grain fusion, with processing methods incorporating high pressures and post pressing sintering. Three routes to achieve this are shown in **Figure 4.1**, with different combinations of pressure and temperature steps. A summary of the ionic conductivity achieved with a range of pressure and temperature fabrication conditions is shown in **Figure 4.1b**.[63,81–84] To achieve the ionic conductivities shown in Figure 1b, an operating pressure of 10s of MPa is typical, with few lower than 10 MPa.[84–89] In a previous report, we compacted commercial argyrodite powders using hot pressing methods and foil electrode contact materials and found the pellet ionic conductivity to be nearly operating pressure invariant, including with a high ionic conductivity at <1 MPa.[88] Here, we replicate this result with our own argyrodite powders and study additional properties of the samples pressed at 150°C, as well as the grain-grain fusion mechanism we hypothesize leads to these results.[88,90]

To quantify how the fabrication conditions (pressure and temperature) and operating conditions (pressure and temperature) affect the pellet (including grain morphology, ionic conductivity, and mechanical properties), we synthesize Li_6PS_5Cl powders using mechanical milling techniques from a previous report.[91] Then, we compact those powders at a fixed pressure of 300 MPa and at two temperatures, 20 °C (by which we mean room temperature) and 150 °C, to form pellets. These temperatures are chosen for comparison with a previous work that used a

commercial argyrodite powder rather than the custom-synthesized powder here.[79] Next, to further explore the differences between the pressing at 20°C and 150°C we evaluate pellet density (which is nearly identical for each temperature), grain morphology, and the ionic conductivity at a range of operating pressures. We assess the pellet mechanical properties through nanoindentation. Through these, we demonstrate that the 150 °C pressing procedure results in retention of the argyrodite crystal structure and chemical composition, a grain morphology (assessed with SEM) that shows enhanced grain-grain fusion, much higher ionic conductivity at <1 MPa operating pressure, and an ionic conductivity with little dependence on operating pressure Nanoindentation experiments indicate the elastic modulus of samples pressed at 150°C is ~2x higher than those pressed at 20°C, while the hardness of each sample is similar. **Figure 4.1c** presents a schematic attributing the differences in ionic conductivity and mechanical properties to enhanced grain-grain fusion for the 150°C compaction process. We hypothesize that at 150°C, with the argyrodite grains softened due to the elevated temperature, there is enhanced mechanical deformation of grain surfaces and grain volumes, resulting in greater grain-grain fusion. The 150°C processing may also redistribute and reduce the presence of any surface contaminants on the initial argyrodite powders at grain-grain interfaces. The enhanced grain-grain fusion for samples pressed at 150°C remains when the pellet is cooled, and results in the changes in the grain morphology, ionic conductivity, and mechanical properties we report in this work. Overall, our demonstration of >2 mS cm^{-1} ionic conductivity at <1 MPa operating pressure with foil electrodes indicates the need to further map the influences of both fabrication temperature and pressure on argyrodite microstructure and properties, and the mechanisms that can result in property retention at commercially relevant operating pressures.

Methods

Synthesis of Li_6PS_5Cl

Li6PS5Cl solid electrolyte was synthesized using a mechanical milling technique.[91] Anhydrous precursors Li2S, P2S5, and LiCl were used as the starting materials to synthesize the Li6PS5Cl solid electrolyte powder. Li2S, P2S5, and LiCl were purchased from sigma Aldrich and was used as received. The molar ratio of Li2S, P2S5, and LiCl is maintained 5:1:2 in their stoichiometric proportions. A mixture of these powders was placed into a ZrO2) ball mill jar (80 mL) in an argon glove box. The solid precursor to ball ratio was maintain 1:4 (by weight). After that the sample was ball mill at 550 rpm for 12 hrs (20 min run 10 min rest). During the process of ball milling the jar was open after every 1h in the glove box and scratch the sample from walls of the ball mill jar. The final powder after ball milling was calcinated in a tubular furnace in Ar atmosphere to 550 °C at 180 °C/h using a custom stainless-steel Swagelok reactor (ID = 6.3 mm, length = 70 mm). Contradictory to the previous report[92,93] where continuous ball milling for 18-20h was used, we stopped the ball milling process after every 1h interval and scratched the precursors which results in more energetic impact on the precursors. We hypothesize that this could be the potential explanation for our success in synthesizing highly crystallized Li_6PS_5Cl powder, which results in high ionic conductivity during pressing at 150°C and chemical stability. The particle size distribution of the Li_6PS_5Cl powder is 0.93 μm with a standard deviation of 0.57 μm. These powders were then packaged and sealed in argon and shipped to the collaborators.

Compaction of the Li_6PS_5Cl Powders

As synthesized Li_6PS_5Cl powder was pressed into pellets between two Cu foils (~15 μm thick) using different amount of powder using a hydraulic press and a temperature-controlled die

set (range 20 °C–250 °C, MTI Corp.) with a diameter of 12.7 mm in an Ar-filled glove box (MBraun). For the hot-pressed pellets, the die set was heated to 150°C then the heating program was turned off to let the die set cool. 300 MPa pressure was used for pellet pressing and it was maintained until the temperature of the die set was below 60 °C. The total time the "hot-pressed" pellets were under pressure was roughly 45 minutes. Cold-pressed pellets were compacted at room temperature (~20°C) and 300 MPa pressure, and the total time the cold-pressed pellets were under pressure was ~5 minutes. The following parameters were used in the fabrication of Li_6PS_5Cl pellets. For pressing temperature control, 20 °C and 150 °C were chosen and referred to as cold and hot pressed respectively. The thickness of each pellet was precisely measured with a micrometer. We measured ionic conductivity using a blocking electrode configuration with a Cu/Li_6PS_5Cl/Cu symmetric cell configuration. The Cu foils were first cut into 12.7 mm in diameter discs then sonically washed in ethanol and fully dried at 80 °C overnight. The Cu foils were included in the pellet pressing step, by first placing a Cu foil at the bottom of the die set, then placing the Li_6PS_5Cl powder, then placing the second Cu foil on top. Hence, the Cu foil electrodes were also included in the pellet compaction process.

Chemical and Morphological Characterization of the Pellets

X-ray photoelectron spectroscopy (XPS) data were collected using a Kratos Ultra DLD XPS system using monochromated Al Kalpha radiation with a photon energy of 1487 eV. Li_6PS_5Cl pellets were transferred directly via UHV transfer from an Ar-filled glovebox to an XPS (Kratos Axis Ultra DLD) system for surface chemical analysis to prevent any air exposure. Survey spectra were collected using a 12 kV monochromatic Al Kα X-ray source in hybrid lens mode with a step size of 1 eV and pass energy of 160 eV. High-resolution spectra were collected using a 12 kV monochromatic Al Kα X-ray source in hybrid lens mode with a step size of 0.1 eV

and pass energy of 20 eV. XPS data were analyzed using the CasaXPS software with quantification performed using peak areas normalized by standard photoionization cross sections corrected for our instrument geometry and a Shirley background for all high-resolution peaks. All spectra were calibrated to the C-C/C-H peak at 285.0 eV.

Scanning electron microscopy (SEM) was done using a Hitachi SU-70 SEM in secondary electron (SE) mode using 10 kV acceleration voltage in the AIMLab at University of Maryland. The samples were hand fractured and transferred to the SEM via Ar-filled glove bags and were only briefly exposed in the air during sample loading for less than 20 s.

The X-ray diffraction spectroscopy (XRD) patterns were measured from 5° to 80° 2θ with step size 0.02° and exposure 0.75 s per step (effective expose was 135 s per step) using Bruker D8 Advance powder diffractometer equipped with Cu anode sealed X-ray tube (CuKα wavelength 1.5418 Å), 0.25° soller slits, Ni β-filter, and LynxEye position sensitive detector.

Ionic Conductivity of the Pellets

The argyrodite pellets with the Cu foil electrodes that were included in the pellet fabrication process were loaded into an MTI Split Coin Cell (Product Code PSC20P). This split cell was assembled with insulating separators and a load cell (HBM U93) into a load frame. Springs purchased from McMaster-Carr (Product #9657K322) were tightened down with the bolts to apply the external load. Spirit levels were utilized to aid in uniaxial application of the mechanical stress. A Biologic SP-300 potentiostat was used to apply potentiostatic electrochemical impedance spectroscopy (PEIS) from 7 MHz to 100 mHz with a 10 mV perturbation potential, taking the average of two points per frequency. The sampling rate was six points per decade. Each PEIS was taken at an initial operating force of 15N, followed by

ascending forces at 50 N increments from 50 N to 1000 N, with the same manner for descending forces. The 15N of force corresponds to just the stainless steel upper die on the sample with no other mechanically induced force on the sample, equivalent to ~0.12 MPa of pressure (the sample diameter is 12.7 mm). Four 20 °C pressed pellets were tested in this manner; three 150° C pressed pellets were also tested, and a fourth 150°C pellet was tested at 15 N followed by 50 N to 950 N at 50 N ascending increments without a subsequent descending measurement. The total time for each measurement and adjusting pressure was roughly 8-10 minutes, resulting in roughly 6 hours to fully test each sample. Each pellet's thickness was measured after the pressure ramp using a VINCA digital micrometer with the Cu foils removed. The ionic conductivity of the pellet system was calculated from the real impedance contribution estimated from the local minima in the spectra before the large tailing associated with the blocking electrode interface and the measured thickness of the respective pellet. Ionic conductivity measurements were done at room temperature (~20°C) unless otherwise noted.

Mechanical Property Characterization

The 150 °C and 20 °C pellets were tested for their Young's modulus and hardness using a Bruker TI Premier nanoindenter inside an Ar glovebox with less than 0.1 ppm O_2 and H_2O. Copper foil that was used in the pressing process was removed from the surface of each pellet and the pellets were glued on to magnetic mounts to minimize tilt and slip during measurement. The pellets were glued on to magnetic mounts to minimize tilt and slip during measurement. A high load transducer with a diamond Berkovich tip was used for all measurements. A maximum load of a 100 mN was used for indentation. This value is much higher than the <5 mN maximum load that is typically used in nanoindentation tests done for sulfide electrolytes [94]. This was done to ensure that surface effects do not influence the nanoindentation behavior, especially because

the pellets were not polished prior to mechanical testing. Several arrays with indents spaced 200 μm apart were used to obtain a total of 66 indents for 20°C and 33 indents for 150 °C pellet. Outliers with a contact depth greater than 5 μm were not included in the analysis.

Results and Discussion

Chemistry and Structure Assessment of the Argyrodite Pellets – XRD and XPS

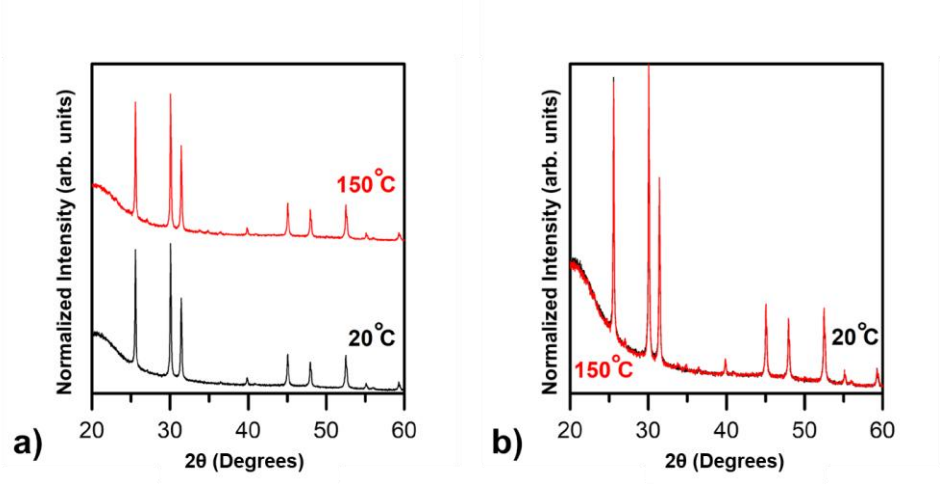

Figure 4.2 XRD of Li_6PS_5Cl pellets. **a)** Stacked and **b)** overlaid normalized XRD patterns of Li_6PS_5Cl pellets pressed at 20 °C and 150 °C.

We performed X-ray diffraction spectroscopy (XRD) measurements to examine the cold pressed (at 20 °C) and hot pressed (at 150 °C) Li_6PS_5Cl pellets for comparing the crystal structures. **Figure 4.2** shows the normalized XRD patterns of the 20 °C and 150 °C samples. As can be seen from both the stacked and overlaid figures, all the characteristic argyrodite peaks match between the 20 °C pressed pellet and 150 °C pellet match, with **Figure 4.2b** notably showing that the backgrounds and normalized peak heights of the 20 °C and 150 °C pellets are nearly identical.[95]

Since the samples that were examined were very similar in terms of sample dimensions, we conclude that the 20 °C and 150 °C pressed Li_6PS_5Cl pellets have the same crystallographic structure. Hence, the differences in the properties of the pellets pressed at 20°C and 150°C do not result from differences in the crystallographic structures.

X-ray Photoelectron Spectroscopy (XPS) Analysis

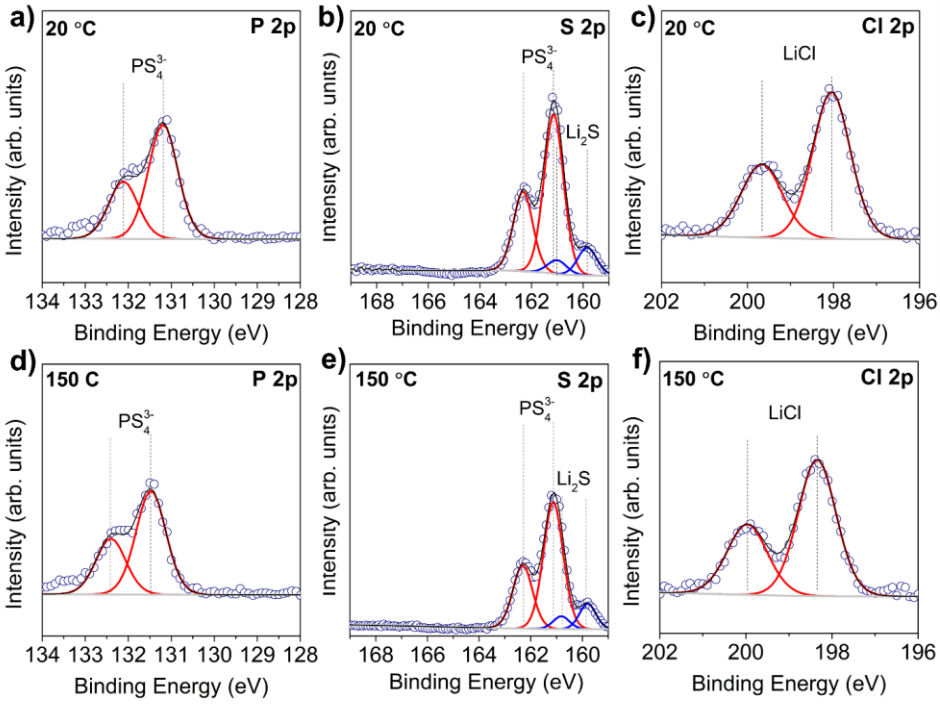

Figure 4.3 XPS of Li_6PS_5Cl pellets. **a)** P 2p, **b)** S 2p, and **c)** Cl 2p high resolution XPS spectra of Li_6PS_5Cl pellets pressed at 20 °C, and **d)** P 2p, **e)** S 2p, and **f)** Cl 2p high resolution XPS spectra of Li_6PS_5Cl pellets pressed at 150 °C. Both pellets were made of 0.24 g of Li_6PS_5Cl powder and pressed at 300 MPa.

We used X-ray photoelectron spectroscopy (XPS) to investigate if the near-pellet-surface chemical composition and bonding of Li_6PS_5Cl differed for the samples pressed at 20°C vs. 150°C. **Figure 4.3** shows the P 2p, S 2p, and Cl 2p high resolution XPS spectra of Li_6PS_5Cl pellets pressed at 20 °C (a), b), and c)) and 150 °C (d), e), and f)). All 2p spectra have spin orbit splitting. As can be seen, there are no additional chemical species or differences in oxidation states between the 20 °C and 150 °C Li_6PS_5Cl pellets. The existence of PS_4^{3-}, Li_2S, and LiCl peaks also agrees with the $Li^+(PS_4^{3-})S^{2-}Cl^-$ ionic formula of Li_6PS_5Cl.[96] In addition, the 2p 3/2 peaks of S, P, and Cl regions are consistent with the binding energies of these constituent elements with shifts of at most 0.1 eV. Hence, pressing at 20°C vs. 150°C did not result in detectable (i.e., >0.1%, the XPS detection limit) differences in the properties of the pellet surfaces measured by XPS.

Morphological Differences in Grain-Grain Contact Assessed with Scanning Electron Microscopy (SEM)

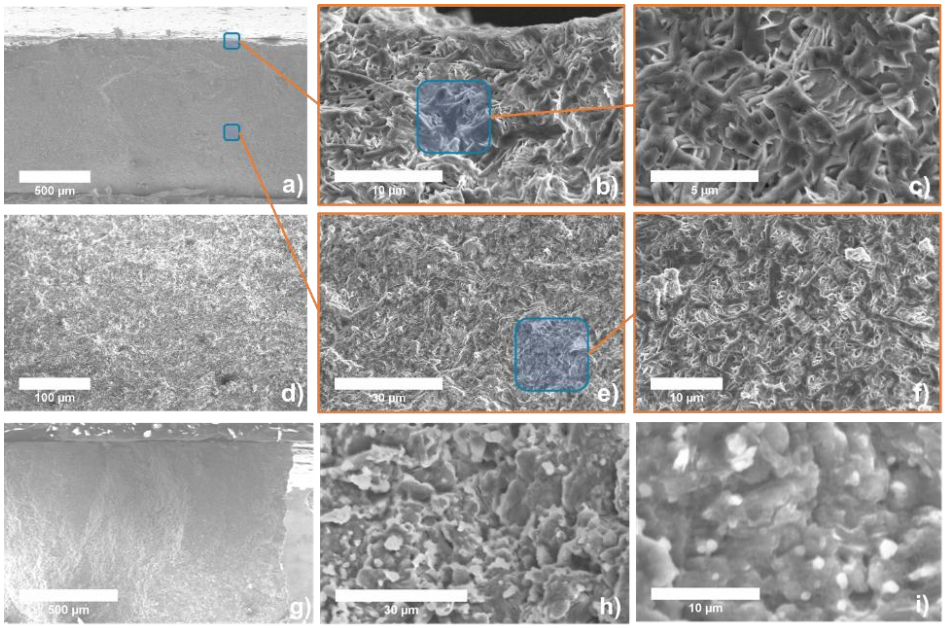

Figure 4.4 SEM cross-sectional images of hand-fractured pellets. Images of 150°C pressed pellets near the pellet surface with scale bars of **(a)** 500 µm, **(b)** 10 µm, and **(c)** 5 µm. Images of 150°C pressed pellets near the pellet center with scale cars of **(d)** 100 µm **(e)** 30 µm and **(f)** 10 µm. Images of 20°C pressed pellets near the pellet center with scale bars of **(g)** 500 µm **(h)** 30 µm and **(i)** 10 µm.

We used scanning electron microscopy (SEM) to examine the fractured cross sections of pellets pressed at 150 °C and 20 °C . The powders from which the pellets were made had an average particle size of 0.93 µm and a standard deviation of 0.57 µm. **Figures 4.4a** to **4.4c** show cross-sectional images near the pellet surface of pellets pressed at 150 °C, while 4d to 4f show images near the pellet center. **Figures 4.4b** and **4.4c** show that the morphology resembles a compressed and entangled web structure with grain-grain fusion. Notably, panels **4.4a** to **4.4f** do not appear to show a significant share of grains that retain the morphology of the initial, individual Li_6PS_5Cl

powders. This indicates that the Li_6PS_5Cl grains were largely "fused" with other grains. On the contrary, **Figure 4.4h** and **4.4i**, which show cross-sectional SEM images of the 20 °C pressed pellet, show a large fraction of grains that appear to retain the original powder morphology, with much less of the web-like structure and grain-grain fusion noted for the 150°C pellets. Overall, the SEM cross-sectional images provide direct visual evidence of enhanced grain-grain fusion for the pellets pressed at 150°C.

Relative Pellet Density

The thickness of each pellet was measured by calipers and the volume calculated from the diameter of the die press (12.7 mm) and the measured mass of the powder. The relative densities of the pellets pressed at 20°C averaged ~88% +/-1.57% (4 samples) and that of the pellets pressed at 150°C averaged ~90% +/- 5.05% (3 samples). We obtained these values using a density of crystalline Li_6PS_5Cl as determined by XRD of 1.83 g cm^{-3}.[89] Hence, the 20°C and 150°C samples have a relative density sufficiently similar that relative density cannot plausibly account for the differences in morphology, ionic conductivity, or mechanical properties. We note that some authors use a crystallographic density of 1.63 g cm^{-3} for Li_6PS_5Cl; this value comes from DFT calculations rather than XRD experiments. If we used 1.63 g cm^{-3} for the crystallographic density we would obtain average relative densities of 98 to 100%, which is not consistent with the SEM images in Figure 4, which indicate some remaining porosity in the samples.[89]

Ionic Conductivity vs. Operating Pressure

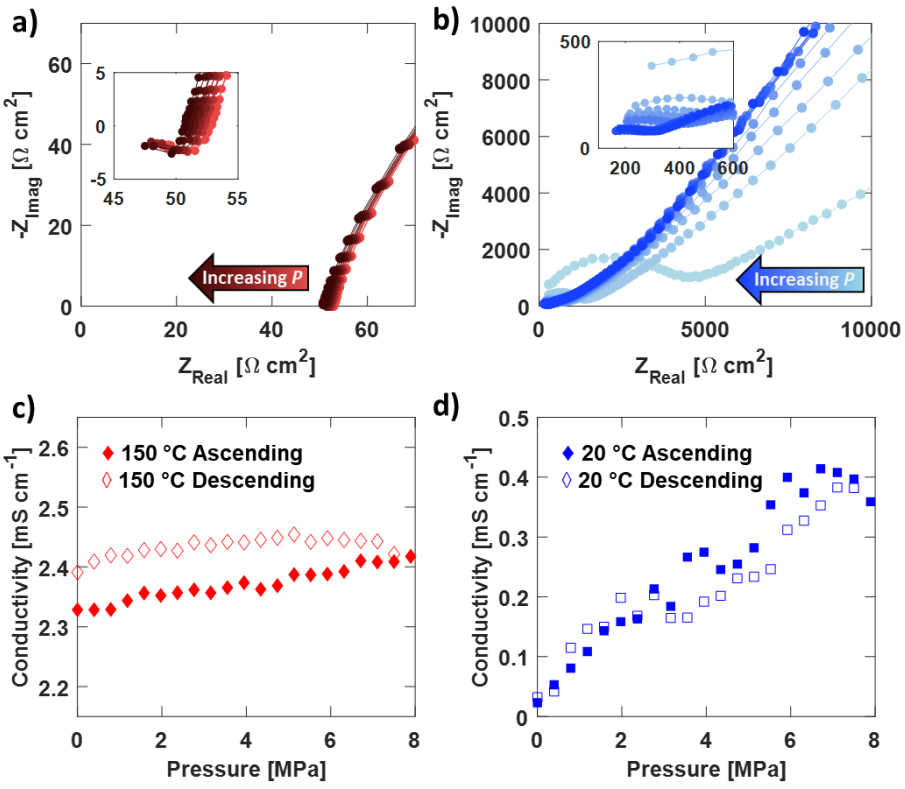

Figure 4.5 Ionic conductivity of pellets at room temperature (~20 °C). **a.** Nyquist plot at 0.8 MPa increments ascending from ~0.12 MPa to ~8 MPa for a pellet pressed at 150 °C **b.** Nyquist plot at 0.8 MPa increments ascending from ~0 0.12 MPa to 8 MPa for a pellet pressed at 20 °C **c.** Ionic conductivity of pellets pressed at 150°C vs. operating pressure **d.** Ionic conductivity of pellets pressed at 20 °C vs operating pressure.

We measured the ionic conductivity of the pellets pressed at 20°C and 150°C vs. operating pressure by placing the pellets in a split cell (Cu foil blocking electrodes are included during the pressing process, so are present on the pellets), and placing the split cell in a load frame with a load cell. We measured at room temperature (~20°C). At each pressure increment (~ 0.4 MPa) the impedance was measured via potentiostatic electrochemical impedance

spectroscopy (PEIS). Each PEIS lasted approximately five minutes with a total time at each pressure of ~10 minutes. Each sample began at ~0.12 MPa, ascended to ~8 MPa at 0.4 MPa increments, and then descended to ~0.12 MPa at equivalent intervals. An implied equivalent circuit model of $R_g(Q_{gb}R_{gb})Q_{Int}$ indicates the local minima value's real impedance before the tailing behavior represents the combined contributions of the grain (R_g) and grain boundaries (R_{gb}). We present the comparison between the equivalent circuit model derived values and the local minima derived ionic conductivities in the Supporting Information (Figure S3). As there is little difference in the calculated ionic conductivity from local minima and the equivalent circuit model results, we conclude that this calculation method is reasonable.

Figure 4.5a-b. displays PEIS at ascending 0.8 MPa increments for a 150 °C pressed sample (**Figure 4.5a.**) and a 20 °C pressed sample (**Figure 4.5b.**). Each sample set displays semicircles in the high frequency region of the impedance spectroscopy (7 MHz to 100 kHz for the 20 °C, 7 MHz to 1 MHz for the 150 °C) before exhibiting large tails indicative of the blocking Cu electrodes. The 150 °C sample PEIS behavior remains nearly invariant with operating pressure, shifting by ~4% in total impedance using the local minima, as well as the impedance at 7 MHz. We hypothesize this is due to the "fused" grains that result from this processing condition. The 20 °C pressed sample (**Figure 4.5b.**) behavior at ~0.12 MPa shows impedance of ~4500 Ohm cm^2 at the local minima, or roughly a 90x increase over the 150 °C pressed sample. The impedance of the 20°C pressed sample strongly depends on the external pressure, falling by ~90% as the pressure increases to 8 MPa. The 7 MHz data point, however, only decreased 37% in impedance from ~0.12 MPa to 8 MPa. This may indicate that a reduction in the grain-grain interface impedance plays a major role in the overall system impedance decrease for the 20°C pressed sample (as shown in **Figure 4.1c**).

The ionic conductivity of the 150 °C pressed samples is higher than that of the 20 °C pressed samples as seen in **Figure 4.5c-d.** Among all samples tested, at ~0.12 MPa the ionic conductivity of the 150 °C pressed samples is ~30x to ~60x greater than that of the 20 °C pressed samples. The ionic conductivity of the 150 °C pressed pellets did not exhibit a strong dependence on the operating pressure whereas for the 20 °C pressed pellets the ionic conductivity increased by ~10x as the operating pressure was increased from ~0.12 MPa to 8 MPa. This behavior was reversible in both the ascending and descending pressure ramps and exhibited a semi-linear response in the 20 °C pressed pellets. Additionally, the semicircle regions associated with grain-grain interactions are greatly reduced in the 150 °C pressed samples even at ~0.12 MPa.

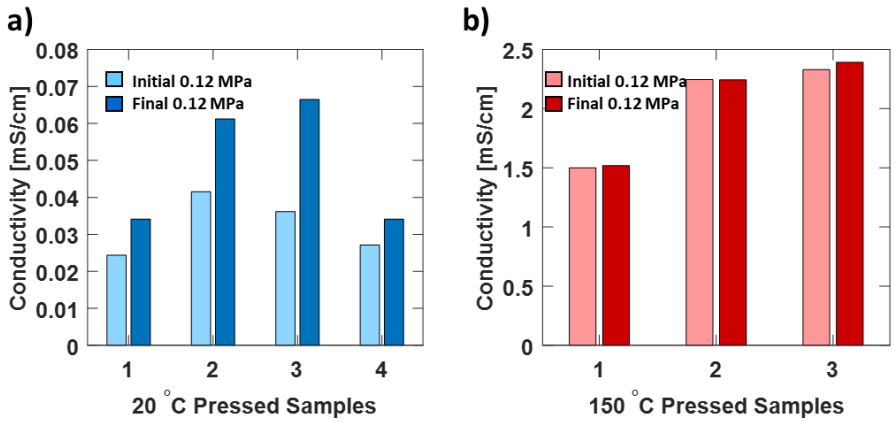

Figure 4.6 Initial and final ionic conductivities at ~20°C and ~0.12 MPa operating pressure across samples (the numbered columns) for the **a.** 20 °C pressed samples and **b.** 150 °C pressed samples.

The reversibility of the ionic conductivity vs. operating pressure results are shown in **Figure 4.6a-b** for four 20 °C and three 150 °C samples**.** The 20 °C pressed samples do not return to the initial ionic conductivity values, but have ionic conductivities that are 30 to 40% higher

than the initial values. This indicates that during the pressure ramp the grain-grain fusion had a slight improvement, although the values for the ionic conductivity for the 20°C pellets remain at >20x lower than of the 150°C pellets. The 150 °C pellets, conversely, showed little change from their initial ionic conductivity to their final ionic conductivity, indicating the grain-grain fusion in the pellets was unaffected by the additional operating pressure ramp for testing ionic conductivity.

The relative densities of the pellets processed at 20°C and 150°C, and the ionic conductivity results in **Figures 4.5** and **4.6**, reinforce the role of a grain-grain fusion mechanism. In particular, while a number of authors have correlated the ionic conductivity of argyrodite pellets with their relative density, in the present case the relative densities differ by only ~2%, which is far too small to account for the >10x difference in ionic conductivity between the 20°C and 150°C pellets based on those published correlations.[89] As shown in the schematic in Figure 1c, we attribute the results in **Figures 4.5** and 4.**6** to differences in how the argyrodite grains are brought into contact, and the potential role of surface contaminants. In particular, for the 150°C case we attribute the higher ionic conductivity, and the lack of dependence of ionic conductivity on operating pressure, to the fusion of adjacent argyrodite grains, which results in direct ionic pathways through the pellet.

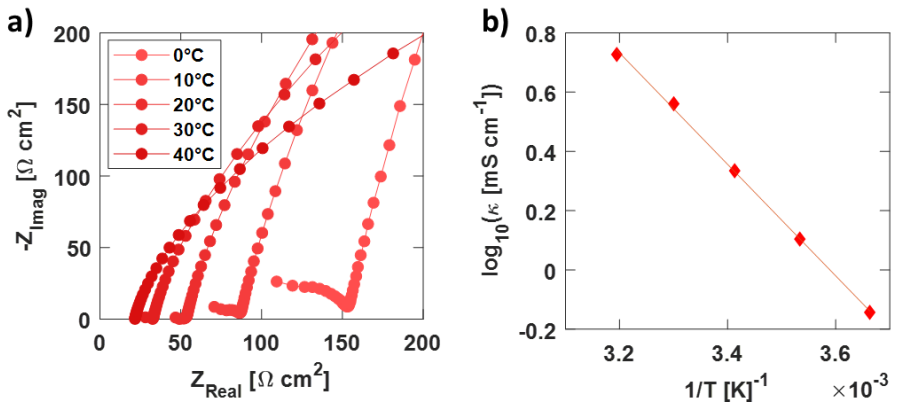

Figure 4.7 Temperature dependent ionic conductivity results at an operating pressure of 0.6 MPa with **a.** the Nyquist plots of the pellets pressed 150 °C and tested at 0 to 40°C at 10°C increments and **b.** the Arrhenius plot of the ionic conductivity vs 1/T. A line is regressed to the data with the slope giving the activation energy.

In addition to our measurements of ionic conductivity at room temperature (reported in Figures 5 and 6), we also measured the ionic conductivity of a 150°C pressed pellet at a fixed pressure over a range of temperatures. We calculate an activation energy of 0.373 eV from the impedance spectroscopy and provide an Arrhenius plot in **Figure 4.7**. The activation energy here is similar to other works that find values in the range of 0.3-0.4 eV for fabrication pressures up to 500 MPa and sintering temperatures from 300 to 400 °C.[81,83,85,97–99] Our results are also similar to some cold pressed methods (e.g., 0.44 eV reported at 670 MPa, 0.31eV for 500 MPa, and 0.40 eV for 340 MPa).[100–104] The spectra in **Figure 4.7a.** may give some insight into the influences contributing to the improved ionic conductivity. As seen in **Figure 4.5b**. the EIS spectra at room temperature of the 20°C pressed pellet has a distinct semicircle feature that is not reflected in the room temperature data of the 150 °C pressed sample. However, as **Figure 4.7a.** shows, this semicircle feature appears at 0 °C. We attribute this semi-circle to grain boundaries

impedance[105], and this indicates the contribution of grain boundaries only becomes apparent for the 150°C pressed sample below room temperature, while the sample pressed at 20°C has this feature present at room temperature.

Mechanical Properties Assessed with Nano-indentation

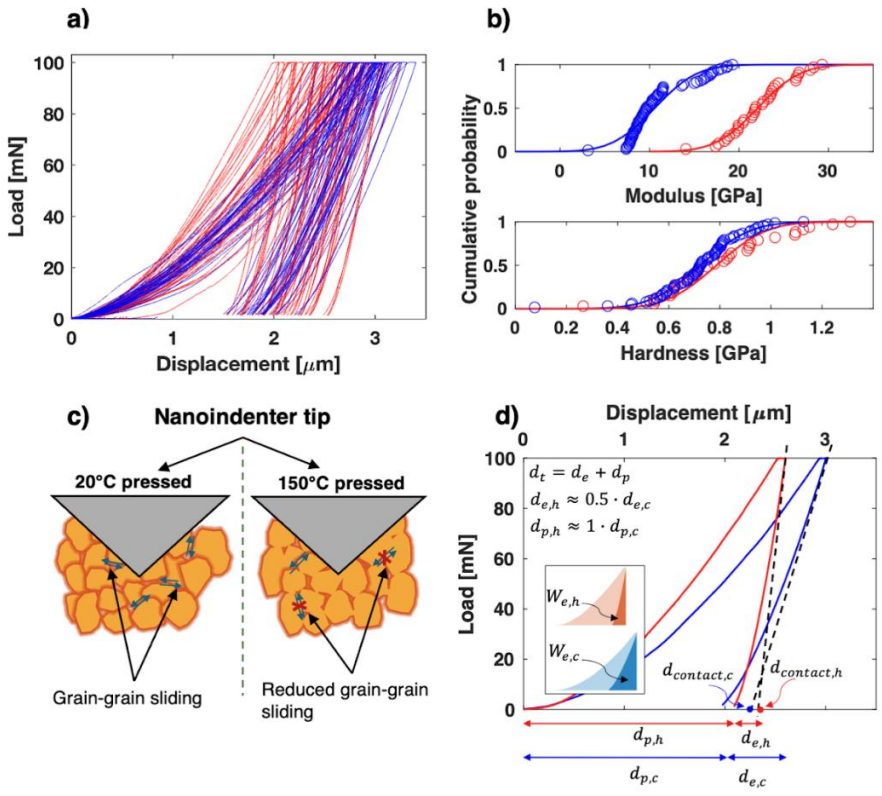

Figure 4.8 Young's modulus and hardness results for a 20 °C and 150 °C pressed pellets measured at ~20°C. A set of 33 indents were done for testing the 150 °C pressed pellet and 66 indents were done for the 20°C pressed pellet. **a.** Load-displacement nanoindentation curves from all indents performed at 100mN for the two cases, **b.** Cumulative

probability functions of the modulus and hardness values. The shape of the fitted curve denotes variation over multiple measurements arising from non-[106]homogeneity in the samples. **c.** Schematic of portions of the pellets directly under the nanoindenter tip showing differences in hypothesized elastic grain-grain sliding during nanoindentation. **d.** Representative nanoindentation curves showing the plastic and elastic deformation in the two cases. d_t is the total or maximum deformation and d_p and d_e are plastic and elastic deformations, respectively. The shaded area under the load-displacement curves denotes the total deformation energy and elastic deformation energy (W_e). Subscripts c and h represent 20°C and 150 °C pellets respectively.

To further understand the effect of the pressing temperature on the pellet properties we measured the mechanical behaviors using a nanoindenter. The Cu foil electrodes were removed prior to the indentation experiments, and no polishing was done. **Figure 4.8a** shows load-displacement curves taken at room temperature for all indents on one pellet pressed at 20°C and one pressed at 150°C. Interestingly, indents on both 20 and 150 °C pressed pellets have similar final displacements at the end of the loading curve (i.e., $d_{p,h} \approx d_{p,c}$, see panel d) for more details), which has implications for the calculated modulus and hardness. The elastic modulus measured though nanoindentation here is the reduced elastic modulus of the sample.

The results in **Figure. 4.8b** show the cumulative probability density (red and blue circles) for the modulus and hardness values obtained from the load-displacement curves shown in **Figure 4.8a**. A normal cumulative density function was fit (shown by solid curves) to the data to evaluate the mean and standard deviation. Significant differences were found in the average elastic moduli for the two pellets. The major difference between the load-displacement curves in blue (20 °C pressed pellet) and red (150°C pressed pellet) shown in Fig. 8a is the slope of the unloading curve which is representative of differences in the elastic behavior of the two pellets. For 150 °C pressed pellet we measured a mean modulus of 22.1 GPa (SD 4.9 GPa) and for the

pellet pressed at 20 °C we measured 10.6 GPa (SD 3.7 GPa). A previous nanoindentation study reports a value of 30 GPa for a hot-pressed Li_6PS_5Cl pellet with a conductivity of 2.9 mS cm^{-1}.[94] A first principles analysis also reports a calculated value of 22 GPa for Li_6PS_5Cl. [107] These values of elastic modulus and ionic conductivity are closer to those we measured for the 150 °C pressed pellet.[94] We believe that the 50% lower observed modulus in the 20°C-pressed pellets vs. the 50°C pressed pellets is indicative of differences in grain-grain fusion.

To elaborate on the role of grain-grain fusion on our results, we note that elastic deformation in polycrystalline materials can arise from differences in the a) intrinsic elastic properties of the grains and grain boundaries, b) relative density (i.e., amount of remaining void volume) and c) grain-grain interactions. [94,108,109] As our XRD results in **Figure 4.3** indicate no differences in pellet crystallinity we conclude that grain elastic properties do not influence the differences we observe. We also know that the relative densities of the two pellets are similar (within 2% on average), therefore, we can also rule out density differences. Instead, our observations here are consistent with previous studies observing grain-grain fusion during sintering in sulfide electrolytes.[110] The grain-grain fusion mechanism can explain the mechanical and electrochemical responses we observe in this work. Grain-grain fusion, in the case of 150 °C pressed pellets, results in reduced elastic grain-grain sliding leading to the observed differences in elastic moduli of the two pellets as shown in the schematic in **Figure 4.8c**. We also note that the average grain size obtained from particle size distribution of the pre-pressed Li_6PS_5Cl powder is 0.93 μm (SD 0.57 μm) and the average maximum displacement (d_t) of all indents obtained at 100mN is ~2.5 μm, so the actual indent size (i.e., size on the surface) is likely to be 15-20 μm. In other words, the indenter tip will mechanically interact with 10s of grains and grain-boundaries. This implies that the 20 °C pellet deforms more elastically via grain-grain

sliding compared to the 150 °C pellet. The observation that grain boundaries decrease the elastic modulus of polycrystalline materials is commonly reported in literature.[111,112] Our work, and the related observations of other authors, indicates more mechanically independent grain boundaries and grain-grain sliding in the 20°C pressed pellets vs. the 150°C pressed pellets.

Figure 4.8d compares the extents of plastic and elastic deformation using a representative indentation load-displacement curve. We observe that the elastic deformation in the 150 °C pressed pellet denoted by $d_{e,h}$ is ~0.5x of the elastic deformation in the 20 °C pellet denoted by $d_{e,c}$, whereas the plastic deformations (non-recoverable parts of the load-displacement curves) denoted by $d_{p,h}$ and $d_{p,c}$ have a similar value. This implies that the 20 °C pellet deforms more elastically through the grain-grain sliding mechanism compared to the 150 °C pressed that has a lower elastic contribution to total deformation. Marx and Blake introduced the use of deformation energy to quantify elastic and plastic deformation, and found that for most elastic-plastic materials the ratio of the elastic deformation energy (obtained by integrating under the unloading curve, shown in Fig 8c as $W_{e,h}$ and $W_{e,c}$) to the total deformation energy (obtained by integrating under the loading curve) is proportional to H/E, where H is hardness and E is the modulus.[106] The ratio of the elastic deformation energy to total deformation energy is 0.2 for the 20 °C pressed pellet and 0.38 for the 150 °C, which is close to the 2x factor observed between the average elastic moduli of the two pellets. Given the ratio of elastic deformation energy to total deformation energy is proportional to H/E, the H values of the two cases studied here must be similar. This is consistent with the calculated hardness shown in Figure 8b. In particular, the 20 °C pressed pellet has a measured hardness 0.72 GPa (± 0.16 GPa) while the 150°C pressed pellet has a value of 0.78 GPa (± 0.25 GPa). Further nanoindentation testing at a range of strain

rates and indentation depths will help to further quantify the mechanical properties of both 20°C and 150°C pressed pellets.

Conclusions

Achieving >2 mS cm^{-1} at <1 MPa operating pressure at room temperature and with foil rather than sputtered electrodes is a demonstration of major significance for practical use of Li_6PS_5Cl argyrodite. To achieve this, we fabricated Li_6PS_5Cl pellets at temperatures of 20°C and 150°C and a pressure of 300 MPa to understand the impact of pressing temperature on pellet morphology, ionic conductivity, and mechanical properties. XRD and XPS measurements confirmed that the structure and composition of the Li_6PS_5Cl remained the same between the 150°C and 20°C samples. SEM imaging showed morphological features resembling smooth, fused structures in the 150 °C samples while pellets pressed at 20 °C did not, instead appearing to retain more un-fused grains. The difference in relative density between pressing conditions is too small to explain the distinct difference in ionic conductivity and modulus. PEIS measurements to determine ionic conductivity and conduction mechanisms showed a reduced impedance associated with the grain-grain interface in the 150 °C samples vs the 20 °C samples. The ionic conductivity of the 150 °C pressed samples does not depend on the operating pressure during testing and is significantly greater than the 20 °C sample as both ~0.12 MPa and at 8 MPa. Nanoindentation results show similar hardness values for each pressing temperature but increased elastic modulus in the 150°C method which is consistent with modulus measurements reported in several studies.[113] We interpret this as reduction of grain sliding through grain fusing in the 150 °C samples. We propose that pressing at 150°C results in more grain fusion than pressing at 20°C, which in turn results in the more fused grain morphology, higher magnitude and operating-pressure-invariant ionic conductivity, and higher elastic modulus. Hence, the “hot

pressing" method studied here is a promising method for argyrodite powder compaction, and additional work to map the pressure-temperature-time-contacts fabrication space that results in high ionic conductivity at <1 MPa operating pressure, and the mechanisms that result in these properties, is recommended. Additional work on how microstructural evolution during fabrication affects grain morphology and properties such as dislocation density and site disorder are promising avenues of exploration.

Overall, a fabrication approach that results in dense samples with high ionic conductivity at <1 MPa operating pressure and foil electrode contacts is a key technological objective, both for separators and cathodes, and our work furthers the measurement of and mechanisms behind Li_6PS_5Cl powder compaction.

ACKNOWLEDGMENTS

This work was supported by the U.S.-Israel Energy Center program managed by the U.S.-Israel Binational Industrial Research and Development (BIRD) Foundation. The authors would like to acknowledge the contributions of Osma Gomez and Adam Antar for the calculation of the density of the material from XRD data and pressing of the pellets. The authors would like to acknowledge and thank Dr. Robert Sacci for his advice given in interpretation of the behaviors of the pellets and Dr. Rupesh Tawari for synthesizing additional samples.

Paper Contributions

Karl Larson was responsible for the electrochemical characterization of the argyrodite pellets and the lead writer of the document. Dr. Yang Wang contributed x-ray analysis through XRD and XPS and Bhuvsmita Bhargava performed the nanoindentation and analysis of the mechanical

properties of the pellets. Argyrodite powders were provided by Dr. Rupesh and Dr. Zitoun from BIU.

Chapter 5: Defining an Ontology for an All Solid-State Battery Database

Introduction

As research scales in response to both demand and influx of additional funding there remains a gap in the research process. The process of meticulously reviewing the literature for all solid-state devices consumes precious time, slowing the pace of research. Review papers are valuable and provide deep insights into the state of the field. However, they are, by nature, static and can be outdated in report in just a few years. This then requires another careful review of the literature and yet another report produced. Further, data science analysis requires a collection and sorting of battery data in one, coherent place. The process of analyzing the state of the solid-state battery research is then impeded by the lack of coherent presentation of the relevant data.

Efforts have arisen to address this issue in other fields and in the realm of electrochemical storage. The U.S. Department of Energy and the European Union both sponsor initiatives in the development of comprehensive battery ontology for lithium-ion technology in the forms of The Battery Data Genome (BDG) and The Battery Interface Genome – Materials Acceleration Program (BIG-MAP), respectively.[114,115] These systems seek to comprehensively collect all information regarding the lithium-ion battery life cycle, from material mining and refining to end of life recycling of the spent batteries. By compiling all relevant information into a single system, they seek to increase the rate of battery research and development.

In this there is room for further development. All solid-state batteries are considered promising next generation in battery technology, allowing energy densities not currently possible in traditional liquid electrolyte chemistries.[116,117] As funding increases in this area of technology so too does the rate of publication.

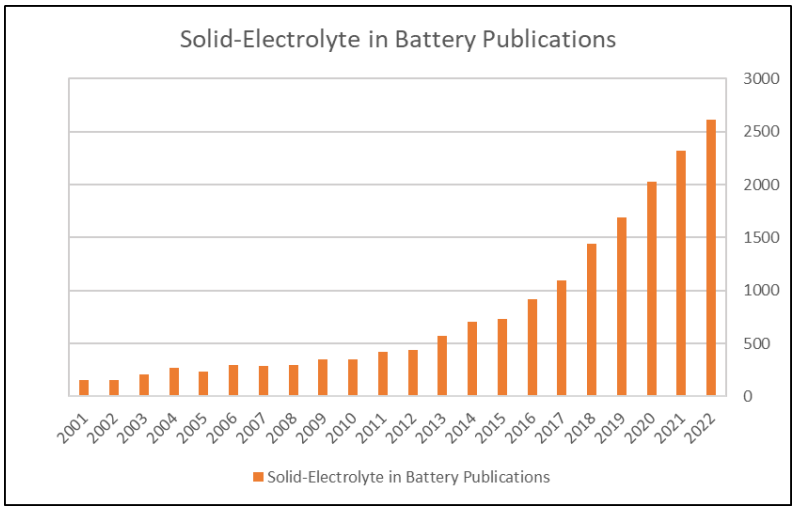

Figure 5.1 Plot of number of battery papers published with "solid electrolytes" from 2001 to 2022, source Web of Science

Figure 5.1 shows the number of publications with the keywords of "solid electrolyte" published from 2001 until 2022. The increase in publications mirrors the increase in funding for batteries by western nations.[118] However, there is, as yet, no solid-state battery analogue to the aforementioned BDG and BIG-MAP systems to capture this growth in research. If the hoped for advances enabled by genomic capture of the field holds true for the Li-ion technology then an analogue must be developed for all solid state chemistries. Here, we discuss our efforts in the design and development of such a system and the challenges inherent to it from the solid-state battery field.

Ontology Layout and Design

The design of our ontology mirrors that of a perovskite database.[119] It is based on the FAIR data principles of Findability, Accessibility, Interoperability, and Reusability. The schema of our system is laid out in the following figure.

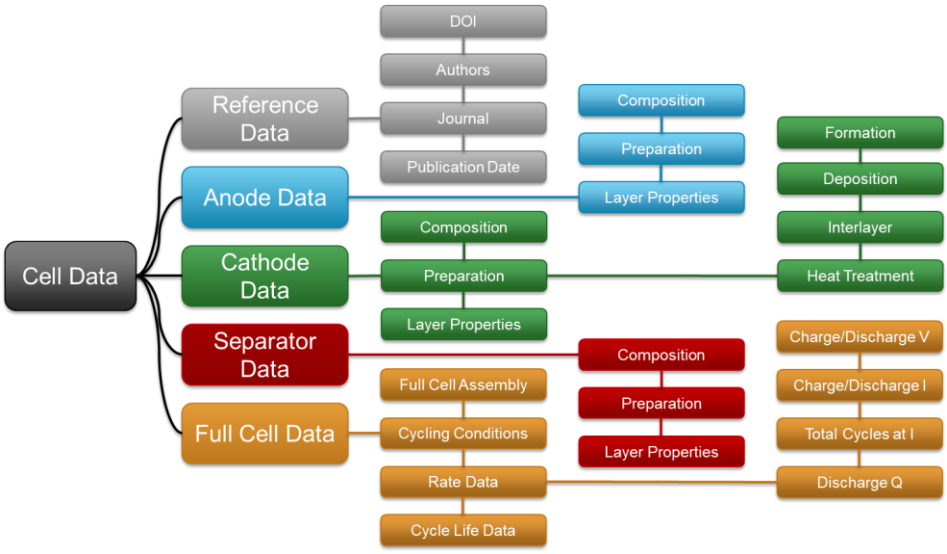

Figure 5.2 Schematic of the ontology layout

Figure 5.2 shows the layout of our proposed ontology. The Findability of the system is represented in the collection and proper reporting of the appropriate metadata of each solid-state battery publication in the system. The first author, journal, publication date, and corresponding DoI are listed for every cell entry. As the system is organized by cell entry and not DoI, this results in multiple entries utilizing the same metadata. Accessibility to the data is ensured through membership in the database, given by our partners in MaterialsZone. The interoperability of the data is preserved as the regular user cannot access or change the data once submitted, allowing extraction, comparison, and analysis as needed without violating the

integrity of the system. Finally, the reusability of the data is ensured through detailed definitions and explanations of the required information for each section of the ontology.

The metadata, named reference data in our system, is but one of five subsections representing the overall electrochemical device. The cell is then made up of the reference data, electrode data (anode and cathode), the separator data, and the performance data given the "Full Cell" section. Each section is composed of multiple subsections, each containing many points of data deemed necessary from the literature.[120] Therein lies a key challenge in designing the ontological framework for the database: useability balanced against exhaustive description. We give one electrode layer as an example.

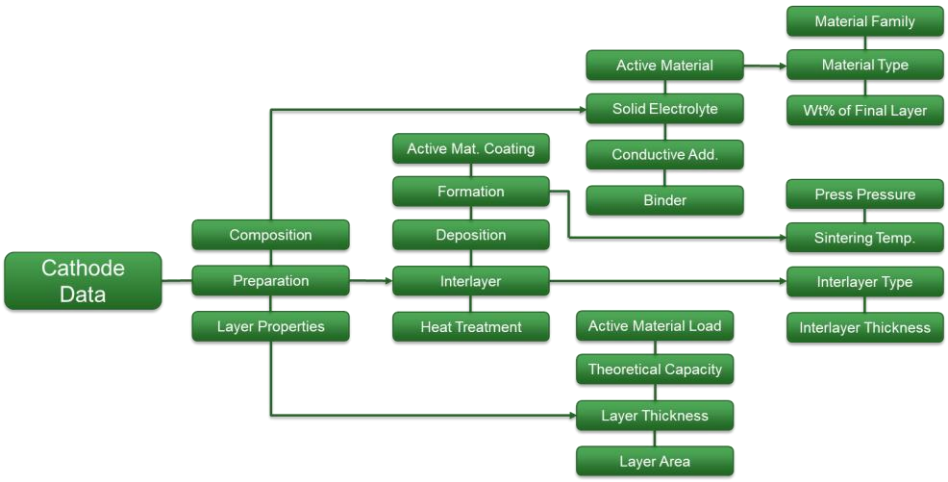

Figure 5.3 Example Schematic of the Cathode layer of the cell, further subdivided into composition, preparation methods, and layer properties.

Figure 5.3 shows a simplified schema of an electrode layer, in this case the cathode. It consists of three subsections, each consisting of further constituent parts. These subsections contain multiple defined data elements and, though simplified, could easily be expanded to dozens more elements

for a more exhaustive description of the electrode layer. Preparation alone requires untold numbers of elements corresponding to the numerous methods by which the cathode layer could be prepared, e.g. hot pressing, doctor blade, etc. While these methods are relevant for understanding in the entirety the performance of the full cell, it is a difficult and daunting barrier to scientists when it comes to data entry. We determined to simplify the system for both data entry purposes and data curation. Currently, the entire ontology exceeds 260 elements for a user to fill out when extracting and uploading data from a paper.

Limitations, Insights, and Future Work

A significant impediment to the extraction of data is the inconsistent reporting practices of the battery research field. As noted by Randau et al., key information vital to contextualizing the performance of the cell is often left unreported in the literature at large.[120] This includes basic information such as the mechanical operating conditions, cell geometries, or even the loading of lithium metal in the full cell configuration. Vargas-Barbosa coordinated an interlaboratory study of argyrodite full cells that noted even the variance in hold times at fabrication pressure resulted in large variance in performance.[121] We observe extensive lack of reporting in many of the same metrics mentioned by Randau et al. and concur with Puls et al. that explicit reporting of all fabrication and operating values be done. Even when certain information is required by journals it is not always enforced by the editors.[114,122] Compounding the issue, there is no standardization in the manner of which data is to be reported. Data is presented in mixed formats of plots, tables, and in the body of the manuscript text. This adds time to the data extraction process as the extractor

We are currently preparing a manuscript detailing our efforts, the observations we made from >250 cells uploaded for analysis, our plans to further improve the database and the user

interface by which data is uploaded. Future iterations will contain robust material list options with the potential to connect with other established databases such as material crystallographic sources. We plan to release the system to the wider battery community to increase the rate of data extraction from the existing literature.

Bibliography

(1) Lou, S.; Zhang, F.; Fu, C.; Chen, M.; Ma, Y.; Yin, G.; Wang, J. Interface Issues and Challenges in All-Solid-State Batteries: Lithium, Sodium, and Beyond. *Advanced Materials* **2021**, *33* (6), 2000721. https://doi.org/10.1002/ADMA.202000721.

(2) York, M.; Larson, K.; Kailot, ·; Harris, C.; Carmona, E.; Albertus, P.; Sharma, R.; Noked, · Malachi; Strauss, E.; Ragones, H.; Golodnitsky, D. Recent Advances in Solid-State beyond Lithium Batteries. *1*, 3. https://doi.org/10.1007/s10008-022-05223-w.

(3) Wang, M.; Wolfenstine, J. B.; Sakamoto, J. Temperature Dependent Flux Balance of the Li/Li7La3Zr2O12 Interface. *Electrochim Acta* **2019**, *296*, 842–847. https://doi.org/10.1016/J.ELECTACTA.2018.11.034.

(4) Jolly, D. S.; Ning, Z.; Darnbrough, J. E.; Kasemchainan, J.; Hartley, G. O.; Adamson, P.; Armstrong, D. E. J.; Marrow, J.; Bruce, P. G. Sodium/Na B" Alumina Interface: Effect of Pressure on Voids. *ACS Appl Mater Interfaces* **2019**, *12* (1), 678–685. https://doi.org/10.1021/ACSAMI.9B17786.

(5) Krauskopf, T.; Hartmann, H.; Zeier, W. G.; Janek, J. Toward a Fundamental Understanding of the Lithium Metal Anode in Solid-State Batteries - An Electrochemo-Mechanical Study on the Garnet-Type Solid Electrolyte Li 6.25 Al 0.25 La 3 Zr 2 O 12. *ACS Appl Mater Interfaces* **2019**, *11* (15), 14463–14477. https://doi.org/10.1021/ACSAMI.9B02537/SUPPL_FILE/AM9B02537_SI_001.PDF.

(6) Du, M.; Sun, Y.; Liu, B.; Chen, B.; Liao, K.; Ran, R.; Cai, R.; Zhou, W.; Shao, Z.; Du, M.; Liu, B.; Liao, K.; Ran, R.; Cai, R.; Zhou, W.; Shao, Z.; Sun, Y.; Chen, B. Smart Construction of an Intimate Lithium | Garnet Interface for All-Solid-State Batteries by Tuning the Tension of Molten Lithium. *Adv Funct Mater* **2021**, *31* (31), 2101556. https://doi.org/10.1002/ADFM.202101556.

(7) Zhang, X.; Wang, Q. J.; Harrison, K. L.; Roberts, S. A.; Harris, S. J. Pressure-Driven Interface Evolution in Solid-State Lithium Metal Batteries. *Cell Rep Phys Sci* **2020**, *1* (2). https://doi.org/10.1016/J.XCRP.2019.100012.

(8) Ortmann, T.; Burkhardt, S.; Eckhardt, J. K.; Fuchs, T.; Ding, Z.; Sann, J.; Rohnke, M.; Ma, Q.; Tietz, F.; Fattakhova-Rohlfing, D.; Kübel, C.; Guillon, O.; Heiliger, C.; Janek, J. Kinetics and Pore Formation of the Sodium Metal Anode on NASICON-Type Na3.4Zr2Si2.4P0.6O12 for Sodium Solid-State Batteries. *Adv Energy Mater* **2023**, *13* (5), 2202712. https://doi.org/10.1002/AENM.202202712.

(9) Wang, M. J.; Choudhury, R.; Sakamoto, J. Characterizing the Li-Solid-Electrolyte Interface Dynamics as a Function of Stack Pressure and Current Density. https://doi.org/10.1016/j.joule.2019.06.017.

(10) Lee, C.; Han, S. Y.; Lewis, J. A.; Shetty, P. P.; Yeh, D.; Liu, Y.; Klein, E.; Lee, H.-W.; Mcdowell, M. T. Stack Pressure Measurements to Probe the Evolution of the Lithium–Solid-State Electrolyte Interface. **2021**. https://doi.org/10.1021/acsenergylett.1c01395.

(11) Flatscher, F.; Philipp, M.; Ganschow, S.; Martin, H.; Wilkening, R.; Rettenwander, D. The Natural Critical Current Density Limit for Li 7 La 3 Zr 2 O 12 Garnets †. **2020**. https://doi.org/10.1039/c9ta14177d.

(12) Deng, T.; Ji, X.; Zhao, Y.; Cao, L.; Li, S.; Hwang, S.; Luo, C.; Wang, P.; Jia, H.; Fan, X.; Lu, X.; Su, D.; Sun, X.; Wang, C.; Zhang, J. G. Tuning the Anode–Electrolyte Interface Chemistry for Garnet-Based Solid-State Li Metal Batteries. *Advanced Materials* **2020**, *32* (23). https://doi.org/10.1002/ADMA.202000030.

(13) Sharafi, A.; Kazyak, E.; Davis, A. L.; Yu, S.; Thompson, T.; Siegel, D. J.; Dasgupta, N. P.; Sakamoto, J. Surface Chemistry Mechanism of Ultra-Low Interfacial Resistance in the Solid-State Electrolyte Li7La3Zr2O12. *Chemistry of Materials* **2017**, *29* (18), 7961–7968. https://doi.org/10.1021/ACS.CHEMMATER.7B03002/ASSET/IMAGES/LARGE/CM-2017-03002V_0005.JPEG.

(14) Dussart, T.; Rividi, N.; Fialin, M.; Toussaint, G.; Stevens, P.; Laberty-Robert, C. Critical Current Density Limitation of LLZO Solid Electrolyte: Microstructure vs Interface. *J Electrochem Soc* **2021**, *168* (12), 120550. https://doi.org/10.1149/1945-7111/AC44BE.

(15) Heo, T. W.; Grieder, A.; Wang, B.; Wood, M.; Hsu, T.; Akhade, S. A.; Wan, L. F.; Chen, L. Q.; Adelstein, N.; Wood, B. C. Microstructural Impacts on Ionic Conductivity of Oxide Solid Electrolytes from a Combined Atomistic-Mesoscale Approach. *npj Computational Materials 2021 7:1* **2021**, *7* (1), 1–15. https://doi.org/10.1038/s41524-021-00681-8.

(16) Jiang, C.; Dunlap, N.; Li, Y.; Guthrey, H.; Liu, P.; Lee, S.; Al-Jassim, M. M. Solid State Electrolytes: Nonuniform Ionic and Electronic Transport of Ceramic and Polymer/Ceramic Hybrid Electrolyte by Nanometer-Scale Operando Imaging for Solid-State Battery (Adv. Energy Mater. 21/2020). *Adv Energy Mater* **2020**, *10* (21), 2070097. https://doi.org/10.1002/AENM.202070097.

(17) Cheng, L.; Chen, W.; Kunz, M.; Persson, K.; Tamura, N.; Chen, G.; Doeff, M. Effect of Surface Microstructure on Electrochemical Performance of Garnet Solid Electrolytes. *ACS Appl Mater Interfaces* **2015**, *7* (3), 2073–2081. https://doi.org/10.1021/AM508111R/SUPPL_FILE/AM508111R_SI_001.PDF.

(18) Buschmann, H.; Berendts, S.; Mogwitz, B.; Janek, J. Lithium Metal Electrode Kinetics and Ionic Conductivity of the Solid Lithium Ion Conductors “Li7La3Zr2O12” and Li7−xLa3Zr2−xTaxO12 with Garnet-Type Structure. *J Power Sources* **2012**, *206*, 236–244. https://doi.org/10.1016/J.JPOWSOUR.2012.01.094.

(19) Krauskopf, T.; Mogwitz, B.; Hartmann, H.; Singh, D. K.; Zeier, W. G.; Janek, J.; Krauskopf, T.; Mogwitz, B.; Hartmann, H.; Singh, D. K.; Zeier, W. G.; Janek, J. The Fast Charge Transfer Kinetics of the Lithium Metal Anode on the Garnet-Type Solid Electrolyte

Li6.25Al0.25La3Zr2O12. *Adv Energy Mater* **2020**, *10* (27), 2000945. https://doi.org/10.1002/AENM.202000945.

(20) Wenzel, S.; Leichtweiss, T.; Weber, D. A.; Sann, J.; Zeier, W. G.; Rgen Janek, J. Interfacial Reactivity Benchmarking of the Sodium Ion Conductors Na 3 PS 4 and Sodium β-Alumina for Protected Sodium Metal Anodes and Sodium All-Solid-State Batteries. **2016**. https://doi.org/10.1021/acsami.6b10119.

(21) Jolly, D. S.; Ning, Z.; Hartley, G. O.; Liu, B.; Melvin, D. L. R.; Adamson, P.; Marrow, J.; Bruce, P. G. Temperature Dependence of Lithium Anode Voiding in Argyrodite Solid-State Batteries. *ACS Appl. Mater. Interfaces* **2021**, *13*, 37. https://doi.org/10.1021/acsami.1c06706.

(22) Kasemchainan, J.; Zekoll, S.; Spencer Jolly, D.; Ning, Z.; Hartley, G. O.; Marrow, J.; Bruce, P. G. Critical Stripping Current Leads to Dendrite Formation on Plating in Lithium Anode Solid Electrolyte Cells. *Nature Materials 2019 18:10* **2019**, *18* (10), 1105–1111. https://doi.org/10.1038/s41563-019-0438-9.

(23) Wang, M. J.; Chang, J. Y.; Wolfenstine, J. B.; Sakamoto, J. Analysis of Elastic, Plastic, and Creep Properties of Sodium Metal and Implications for Solid-State Batteries. *Materialia (Oxf)* **2020**, *12*, 100792. https://doi.org/10.1016/J.MTLA.2020.100792.

(24) Masias, A.; Felten, N.; Garcia-Mendez, R.; Wolfenstine, J.; Sakamoto, J. Elastic, Plastic, and Creep Mechanical Properties of Lithium Metal. *Journal of Materials Science 2018 54:3* **2018**, *54* (3), 2585–2600. https://doi.org/10.1007/S10853-018-2971-3.

(25) Masias, A.; Felten, N.; Garcia-Mendez, R.; Wolfenstine, J.; Sakamoto, J. Elastic, Plastic, and Creep Mechanical Properties of Lithium Metal. *J Mater Sci* **2019**, *54* (3), 2585–2600. https://doi.org/10.1007/S10853-018-2971-3/METRICS.

(26) Haslam, C. G.; Wolfenstine, J. B.; Sakamoto, J. The Effect of Aspect Ratio on the Mechanical Behavior of Li Metal in Solid-State Cells. *J Power Sources* **2022**, *520*, 230831. https://doi.org/10.1016/J.JPOWSOUR.2021.230831.

(27) Bay, M.-C.; Wang, M.; Grissa, R.; F Heinz, M. V; Sakamoto, J.; Battaglia, C.; Bay, M.; Grissa, R.; F Heinz, M. V; Battaglia Empa, C.; Wang, M.; Sakamoto, J. Sodium Plating from Na-B"-Alumina Ceramics at Room Temperature, Paving the Way for Fast-Charging All-Solid-State Batteries. *Adv Energy Mater* **2020**, *10* (3), 1902899. https://doi.org/10.1002/AENM.201902899.

(28) Doering, M.; Kieninger, J.; Kübler, J.; -, al; Wang, L.; Hartmann, P.; Donkó, Z. Three-Electrode Setups for Lithium-Ion Batteries. *J Electrochem Soc* **2016**, *164* (2), A80. https://doi.org/10.1149/2.0241702JES.

(29) Li, Z.; Zhao, L.; Jiang, Z. Three-Electrode Setups for Lithium-Ion Batteries. *J Electrochem Soc* **2016**, *164* (2), A71. https://doi.org/10.1149/2.0231702JES.

(30) Dollé, M.; Orsini, F.; Gozdz, A. S.; Tarascon, J.-M. Development of Reliable Three-Electrode Impedance Measurements in Plastic Li-Ion Batteries. *J Electrochem Soc* **2001**, *148* (8), A851. https://doi.org/10.1149/1.1381071/XML.

(31) Ning, Z.; Li, G.; Melvin, D. L. R.; Chen, Y.; Bu, J.; Spencer-Jolly, D.; Liu, J.; Hu, B.; Gao, X.; Perera, J.; Gong, C.; Pu, S. D.; Zhang, S.; Liu, B.; Hartley, G. O.; Bodey, A. J.; Todd, R. I.; Grant, P. S.; Armstrong, D. E. J.; Marrow, T. J.; Monroe, C. W.; Bruce, P. G. Dendrite Initiation and Propagation in Lithium Metal Solid-State Batteries. *Nature 2023 618:7964* **2023**, *618* (7964), 287–293. https://doi.org/10.1038/s41586-023-05970-4.

(32) Zaman, W.; Zhao, L.; Martin, T.; Zhang, X.; Wang, Z.; Wang, Q. J.; Harris, S.; Hatzell, K. B. Temperature and Pressure Effects on Unrecoverable Voids in Li Metal Solid-State Batteries. *ACS Appl Mater Interfaces* **2023**, *15* (31), 37401–37409. https://doi.org/10.1021/ACSAMI.3C05886/ASSET/IMAGES/LARGE/AM3C05886_0006.JPEG.

(33) Spencer Jolly, D.; Ning, Z.; Hartley, G. O.; Liu, B.; Melvin, D. L. R.; Adamson, P.; Marrow, J.; Bruce, P. G. Temperature Dependence of Lithium Anode Voiding in Argyrodite Solid-State Batteries. *ACS Appl Mater Interfaces* **2021**, *13* (19), 22708–22716. https://doi.org/10.1021/ACSAMI.1C06706/ASSET/IMAGES/LARGE/AM1C06706_0007.JPEG.

(34) Jiang, Y.; Zhu, X.; Lai, W. Three Electrodes Analysis of a 3 V-Class All-Solid-State Lithium-Ion Battery Based on Garnet-Type Solid Electrolyte Li6.4La3Zr1.4Ta0.6O12. *J Power Sources* **2022**, *529*, 231278. https://doi.org/10.1016/J.JPOWSOUR.2022.231278.

(35) Chang, G. H.; Choi, H. U.; Kang, S.; Park, J. Y.; Lim, H. T. Characterization of Limiting Factors of an All-Solid-State Li-Ion Battery Using an Embedded Indium Reference Electrode. *Ionics (Kiel)* **2020**, *26* (3), 1555–1561. https://doi.org/10.1007/S11581-019-03367-W/TABLES/1.

(36) Dugas, R.; Dupraz, Y.; Quemin, E.; Koç, T.; Tarascon, J.-M. Engineered Three-Electrode Cells for Improving Solid State Batteries. *J Electrochem Soc* **2021**, *168* (9), 090508. https://doi.org/10.1149/1945-7111/AC208D.

(37) Koç, T.; Hallot, M.; Quemin, E.; Hennequart, B.; Dugas, R.; Abakumov, A. M.; Lethien, C.; Tarascon, J. M. Toward Optimization of the Chemical/Electrochemical Compatibility of Halide Solid Electrolytes in All-Solid-State Batteries. *ACS Energy Lett* **2022**, *7* (9), 2979–2987. https://doi.org/10.1021/ACSENERGYLETT.2C01668/ASSET/IMAGES/LARGE/NZ2C01668_0006.JPEG.

(38) Sharafi, A.; Meyer, H. M.; Nanda, J.; Wolfenstine, J.; Sakamoto, J. Characterizing the Li–Li7La3Zr2O12 Interface Stability and Kinetics as a Function of Temperature and Current Density. *J Power Sources* **2016**, *302*, 135–139. https://doi.org/10.1016/J.JPOWSOUR.2015.10.053.

(39) Fu, K.; Gong, Y.; Hitz, G. T.; McOwen, D. W.; Li, Y.; Xu, S.; Wen, Y.; Zhang, L.; Wang, C.; Pastel, G.; Dai, J.; Liu, B.; Xie, H.; Yao, Y.; Wachsman, E. D.; Hu, L. Three-Dimensional Bilayer Garnet Solid Electrolyte Based High Energy Density Lithium Metal–Sulfur Batteries. *Energy Environ Sci* **2017**, *10* (7), 1568–1575. https://doi.org/10.1039/C7EE01004D.

(40) Armstrong, R. D.; Sellick, D. P. A. c. Impedance Studies on Sodium β-Alumina Tubes for Use in Sodium-Sulphur Cells. *J Appl Electrochem* **1979**, *9* (5), 623–628. https://doi.org/10.1007/BF00610950/METRICS.

(41) Archer, W. I.; Armstrong, R. D.; Sellick, D. P.; Bugden, W. G.; Duncan, J. H. The Relationship between the a.c. Impedance and Microstructure of a Sodium β-Alumina Ceramic. *J Mater Sci* **1980**, *15* (8), 2066–2072. https://doi.org/10.1007/BF00550633/METRICS.

(42) Carmona, E. A.; Albertus, P. Modeling How Interface Geometry and Mechanical Stress Affect Li Metal / Solid Electrolyte Current Distributions. *J Electrochem Soc* **2023**. https://doi.org/10.1149/1945-7111/ACB8E3.

(43) Liu, B.; Zhang, L.; Xu, S.; McOwen, D. W.; Gong, Y.; Yang, C.; Pastel, G. R.; Xie, H.; Fu, K.; Dai, J.; Chen, C.; Wachsman, E. D.; Hu, L. 3D Lithium Metal Anodes Hosted in Asymmetric Garnet Frameworks toward High Energy Density Batteries. *Energy Storage Mater* **2018**, *14*, 376–382. https://doi.org/10.1016/J.ENSM.2018.04.015.

(44) Lim, G. J. H.; Lyu, Z.; Zhang, X.; Koh, J. J.; Zhang, Y.; He, C.; Adams, S.; Wang, J.; Ding, J. Robust Pure Copper Framework by Extrusion 3D Printing for Advanced Lithium Metal Anodes. *J Mater Chem A Mater* **2020**, *8* (18), 9058–9067. https://doi.org/10.1039/D0TA00209G.

(45) Zhang, Y.; Wang, C.; Pastel, G.; Kuang, Y.; Xie, H.; Li, Y.; Liu, B.; Luo, W.; Chen, C.; Hu, L.; Zhang, Y.; Wang, C.; Pastel, G.; Kuang, Y.; Xie, H.; Li, Y.; Liu, B.; Luo, W.; Chen, C.; Hu, L. 3D Wettable Framework for Dendrite-Free Alkali Metal Anodes. *Adv Energy Mater* **2018**, *8* (18), 1800635. https://doi.org/10.1002/AENM.201800635.

(46) Hu, X.; Zhang, Z.; Zhang, X.; Wang, Y.; Yang, X.; Wang, X.; Fayena-Greenstein, M.; Yehezkel, H. A.; Langford, S.; Zhou, D.; Li, B.; Wang, G.; Aurbach, D. External-Pressure–Electrochemistry Coupling in Solid-State Lithium Metal Batteries. *Nature Reviews Materials 2024 9:5* **2024**, *9* (5), 305–320. https://doi.org/10.1038/s41578-024-00669-y.

(47) Tseng, K. T.; Lee, K.; Sakamoto, J. Enabling "Sodium-Metal-Free" Manufacturing of Solid-State Batteries. *ACS Energy Lett* **2024**, *22*, 4544–4549. https://doi.org/10.1021/ACSENERGYLETT.4C01724/ASSET/IMAGES/LARGE/NZ4C01724_0003.JPEG.

(48) Ham, S. Y.; Yang, H.; Nunez-cuacuas, O.; Tan, D. H. S.; Chen, Y. T.; Deysher, G.; Cronk, A.; Ridley, P.; Doux, J. M.; Wu, E. A.; Jang, J.; Meng, Y. S. Assessing the Critical Current Density of All-Solid-State Li Metal Symmetric and Full Cells. *Energy Storage Mater* **2023**, *55*, 455–462. https://doi.org/10.1016/J.ENSM.2022.12.013.

(49) Zhang, X.; Wang, Q. J.; Harrison, K. L.; Roberts, S. A.; Harris, S. J. Pressure-Driven Interface Evolution in Solid-State Lithium Metal Batteries. *Cell Rep Phys Sci* **2020**, *1* (2), 100012. https://doi.org/10.1016/J.XCRP.2019.100012.

(50) Xu, H.; Yang, S.; Li, B. Pressure Effects and Countermeasures in Solid-State Batteries: A Comprehensive Review. *Adv Energy Mater* **2024**, *14* (16), 2303539. https://doi.org/10.1002/AENM.202303539.

(51) Doux, J.-M.; Nguyen, H.; S Tan, D. H.; Banerjee, A.; Wang, X.; Wu, E. A.; Jo, C.; Yang, H.; Shirley Meng, Y.; Doux, J.; Nguyen, H.; S Tan, D. H.; Banerjee, A.; Wang, X.; Wu, E. A.; Jo, C.; Yang, H.; Meng, Y. S. Stack Pressure Considerations for Room-Temperature All-Solid-State

Lithium Metal Batteries. *Adv Energy Mater* **2020**, *10* (1), 1903253. https://doi.org/10.1002/AENM.201903253.

(52) Sakamoto, J. More Pressure Needed. *Nature Energy 2019 4:10* **2019**, *4* (10), 827–828. https://doi.org/10.1038/s41560-019-0478-z.

(53) Lee, K.; Sakamoto, J. Li Stripping Behavior of Anode-Free Solid-State Batteries Under Intermittent-Current Discharge Conditions. *Adv Energy Mater* **2024**, *14* (17), 2303571. https://doi.org/10.1002/AENM.202303571.

(54) Zhang, F.; Guo, Y.; Zhang, L.; Jia, P.; Liu, X.; Qiu, P.; Zhang, H.; Huang, J. A Review of the Effect of External Pressure on All-Solid-State Batteries. *eTransportation* **2023**, *15*, 100220. https://doi.org/10.1016/J.ETRAN.2022.100220.

(55) Doux, J. M.; Nguyen, H.; Tan, D. H. S.; Banerjee, A.; Wang, X.; Wu, E. A.; Jo, C.; Yang, H.; Meng, Y. S. Stack Pressure Considerations for Room-Temperature All-Solid-State Lithium Metal Batteries. *Adv Energy Mater* **2020**, *10* (1). https://doi.org/10.1002/AENM.201903253.

(56) Yin, X.; Tang, W.; Jung, I. D.; Phua, K. C.; Adams, S.; Lee, S. W.; Zheng, G. W. Insights into Morphological Evolution and Cycling Behaviour of Lithium Metal Anode under Mechanical Pressure. *Nano Energy* **2018**, *50*, 659–664. https://doi.org/10.1016/j.nanoen.2018.06.003.

(57) Wang, Y.; Liu, T.; Kumar, J. Effect of Pressure on Lithium Metal Deposition and Stripping against Sulfide-Based Solid Electrolytes. *ACS Appl Mater Interfaces* **2020**, *12* (31), 34771–34776. https://doi.org/10.1021/ACSAMI.0C06201/ASSET/IMAGES/LARGE/AM0C06201_0004.JPEG.

(58) Cao, D.; Ji, T.; Wei, Z.; Liang, W.; Bai, R.; Burch, K. S.; Geiwitz, M.; Zhu, H. Enhancing Lithium Stripping Efficiency in Anode-Free Solid-State Batteries through Self-Regulated Internal Pressure. *Nano Lett* **2023**, *23* (20), 9392–9398. https://doi.org/10.1021/ACS.NANOLETT.3C02713/ASSET/IMAGES/LARGE/NL3C02713_0005.JPEG.

(59) Asakura, T.; Inaoka, T.; Hotehama, C.; Kowada, H.; Motohashi, K.; Sakuda, A.; Tatsumisago, M.; Hayashi, A. Stack Pressure Dependence of Li Stripping/Plating Performance in All-Solid-State Li Metal Cells Containing Sulfide Glass Electrolytes. *ACS Appl Mater Interfaces* **2023**, *15* (26), 31403–31408. https://doi.org/10.1021/ACSAMI.3C03552/ASSET/IMAGES/LARGE/AM3C03552_0005.JPEG.

(60) Larson, K.; Carmona, E. A.; Albertus, P. Reference Electrode Reveals Insights on Sodium Metal/Solid Electrolyte Interface Cycling and Voiding Behaviors at High Current Densities and Areal Capacities. *ACS Appl Mater Interfaces* **2023**, *15* (42), 49213–49222. https://doi.org/10.1021/ACSAMI.3C10933/ASSET/IMAGES/LARGE/AM3C10933_0007.JPEG.

(61) Wang, M. J.; Chang, J. Y.; Wolfenstine, J. B.; Sakamoto, J. Analysis of Elastic, Plastic, and Creep Properties of Sodium Metal and Implications for Solid-State Batteries. *Materialia (Oxf)* **2020**, *12*, 100792. https://doi.org/10.1016/J.MTLA.2020.100792.

(62) Hartel, J.; Banik, A.; Gerdes, J. M.; Wankmiller, B.; Helm, B.; Li, C.; Kraft, M. A.; Hansen, M. R.; Zeier, W. G. Understanding Lithium-Ion Transport in Selenophosphate-Based Lithium Argyrodites and Their Limitations in Solid-State Batteries. *Chemistry of Materials* **2023**, *35* (12), 4798–4809. https://doi.org/10.1021/ACS.CHEMMATER.3C00658/SUPPL_FILE/CM3C00658_SI_002.ZIP.

(63) Zhou, L.; Minafra, N.; Zeier, W. G.; Nazar, L. F. Innovative Approaches to Li-Argyrodite Solid Electrolytes for All-Solid-State Lithium Batteries. *Acc Chem Res* **2021**, *54* (12), 2717–2728. https://doi.org/10.1021/ACS.ACCOUNTS.0C00874/ASSET/IMAGES/LARGE/AR0C00874_0006.JPEG.

(64) Yu, C.; Zhao, F.; Luo, J.; Zhang, L.; Sun, X. Recent Development of Lithium Argyrodite Solid-State Electrolytes for Solid-State Batteries: Synthesis, Structure, Stability and Dynamics. *Nano Energy* **2021**, *83*, 105858. https://doi.org/10.1016/j.nanoen.2021.105858.

(65) Brinek, M.; Hiebl, C.; Wilkening, H. M. R. Understanding the Origin of Enhanced Li-Ion Transport in Nanocrystalline Argyrodite-Type Li6PS5I. *Chemistry of Materials* **2020**, *32* (11), 4754–4766. https://doi.org/10.1021/ACS.CHEMMATER.0C01367/ASSET/IMAGES/LARGE/CM0C01367_0008.JPEG.

(66) Peng, L.; Yu, C.; Cheng, S.; Xie, J. Halogen-Rich Lithium Argyrodite Solid-State Electrolytes: A Review. *Batter Supercaps* **2023**, *6* (5), e202200553. https://doi.org/10.1002/BATT.202200553.

(67) Zaman, W.; Hatzell, K. B. Processing and Manufacturing of next Generation Lithium-Based All Solid-State Batteries. *Curr Opin Solid State Mater Sci* **2022**, *26* (4), 101003. https://doi.org/10.1016/J.COSSMS.2022.101003.

(68) Yu, C.; Zhao, F.; Luo, J.; Zhang, L.; Sun, X. Recent Development of Lithium Argyrodite Solid-State Electrolytes for Solid-State Batteries: Synthesis, Structure, Stability and Dynamics. *Nano Energy* **2021**, *83*, 105858. https://doi.org/10.1016/J.NANOEN.2021.105858.

(69) Zhang, Z.; Zhang, L.; Liu, Y.; Yan, X.; Xu, B.; Wang, L. min. One-Step Solution Process toward Formation of Li6PS5Cl Argyrodite Solid Electrolyte for All-Solid-State Lithium-Ion Batteries. *J Alloys Compd* **2020**, *812*, 152103. https://doi.org/10.1016/J.JALLCOM.2019.152103.

(70) Ning, Z.; Li, G.; Melvin, D. L. R.; Chen, Y.; Bu, J.; Spencer-Jolly, D.; Liu, J.; Hu, B.; Gao, X.; Perera, J.; Gong, C.; Pu, S. D.; Zhang, S.; Liu, B.; Hartley, G. O.; Bodey, A. J.; Todd, R. I.; Grant, P. S.; Armstrong, D. E. J.; Marrow, T. J.; Monroe, C. W.; Bruce, P. G. Dendrite Initiation and Propagation in Lithium Metal Solid-State Batteries. *Nature 2023 618:7964* **2023**, *618* (7964), 287–293. https://doi.org/10.1038/s41586-023-05970-4.

(71) Faka, V.; Agne, M. T.; Lange, M. A.; Daisenberger, D.; Wankmiller, B.; Schwarzmüller, S.; Huppertz, H.; Maus, O.; Helm, B.; Böger, T.; Hartel, J.; Gerdes, J. M.; Molaison, J. J.; Kieslich, G.; Hansen, M. R.; Zeier, W. G. Pressure-Induced Dislocations and Their Influence on Ionic Transport in Li+-Conducting Argyrodites. *J Am Chem Soc* **2024**, *146* (2), 1710–1721. https://doi.org/10.1021/JACS.3C12323/ASSET/IMAGES/LARGE/JA3C12323_0008.JPEG.

(72) Subramanian, Y.; Rajagopal, R.; Ryu, K. S. Blending a Li3N/Li3YCl6 Solid Electrolyte with Li6PS5Cl Argyrodite Structure to Improve Interface Stability and Electrochemical Performance in Lithium Solid-State Batteries. *J Alloys Compd* **2023**, *940*, 168867. https://doi.org/10.1016/J.JALLCOM.2023.168867.

(73) Doux, J. M.; Yang, Y.; Tan, D. H. S.; Nguyen, H.; Wu, E. A.; Wang, X.; Banerjee, A.; Meng, Y. S. Pressure Effects on Sulfide Electrolytes for All Solid-State Batteries. *J Mater Chem A Mater* **2020**, *8* (10), 5049–5055. https://doi.org/10.1039/C9TA12889A.

(74) Kim, K. J.; Balaish, M.; Wadaguchi, M.; Kong, L.; Rupp, J. L. M.; Kim, K. J.; Balaish, M.; Kong, L.; Rupp, L. M.; Wadaguchi, M. Solid-State Li–Metal Batteries: Challenges and Horizons of Oxide and Sulfide Solid Electrolytes and Their Interfaces. *Adv Energy Mater* **2021**, *11* (1), 2002689. https://doi.org/10.1002/AENM.202002689.

(75) Jiang, P.; Du, G.; Cao, J.; Zhang, X.; Zou, C.; Liu, Y.; Lu, X. Solid-State Li Ion Batteries with Oxide Solid Electrolytes: Progress and Perspective. *Energy Technology* **2023**, *11* (3), 2201288. https://doi.org/10.1002/ENTE.202201288.

(76) Wei, R.; Chen, S.; Gao, T.; Liu, W. Challenges, Fabrications and Horizons of Oxide Solid Electrolytes for Solid-State Lithium Batteries. *Nano Select* **2021**, *2* (12), 2256–2274. https://doi.org/10.1002/NANO.202100110.

(77) Cronau, M.; Szabo, M.; König, C.; Wassermann, T. B.; Roling, B. How to Measure a Reliable Ionic Conductivity? The Stack Pressure Dilemma of Microcrystalline Sulfide-Based Solid Electrolytes. *ACS Energy Lett* **2021**, *6* (9), 3072–3077. https://doi.org/10.1021/ACSENERGYLETT.1C01299/ASSET/IMAGES/LARGE/NZ1C01299_0005.JPEG.

(78) Hänsel, C.; Kundu, D.; Hänsel, C.; Kundu, D. The Stack Pressure Dilemma in Sulfide Electrolyte Based Li Metal Solid-State Batteries: A Case Study with Li6PS5Cl Solid Electrolyte. *Adv Mater Interfaces* **2021**, *8* (10), 2100206. https://doi.org/10.1002/ADMI.202100206.

(79) Wang, Y.; Hoang, B.; Hoerauf, J.; Lee, C.; Lin, C.-F.; Rubloff, G. W.; Lee, S. B.; Kozen, A. C. Hot and Cold Pressed LGPS Solid Electrolytes. *J Electrochem Soc* **2021**, *168* (1), 010533. https://doi.org/10.1149/1945-7111/ABDB44.

(80) Albertus, P.; Anandan, V.; Ban, C.; Balsara, N.; Belharouak, I.; Buettner-Garrett, J.; Chen, Z.; Daniel, C.; Doeff, M.; Dudney, N. J.; Dunn, B.; Harris, S. J.; Herle, S.; Herbert, E.; Kalnaus, S.; Libera, J. A.; Lu, D.; Martin, S.; McCloskey, B. D.; McDowell, M. T.; Meng, Y. S.; Nanda, J.; Sakamoto, J.; Self, E. C.; Tepavcevic, S.; Wachsman, E.; Wang, C.; Westover, A. S.; Xiao, J.; Yersak, T. Challenges for and Pathways toward Li-Metal-Based All-Solid-State Batteries. *ACS Energy Lett* **2021**, *6* (4), 1399–1404. https://doi.org/10.1021/ACSENERGYLETT.1C00445/ASSET/IMAGES/LARGE/NZ1C00445_0003.JPEG.

(81) Wang, S.; Zhang, Y.; Zhang, X.; Liu, T.; Lin, Y. H.; Shen, Y.; Li, L.; Nan, C. W. High-Conductivity Argyrodite Li 6 PS 5 Cl Solid Electrolytes Prepared via Optimized Sintering Processes for All-

Solid-State Lithium-Sulfur Batteries. *ACS Appl Mater Interfaces* **2018**, *10* (49), 42279–42285. https://doi.org/10.1021/ACSAMI.8B15121/ASSET/IMAGES/LARGE/AM-2018-151213_0007.JPEG.

(82) Kasemchainan, J.; Zekoll, S.; Spencer Jolly, D.; Ning, Z.; Hartley, G. O.; Marrow, J.; Bruce, P. G. Critical Stripping Current Leads to Dendrite Formation on Plating in Lithium Anode Solid Electrolyte Cells. *Nature Materials 2019 18:10* **2019**, *18* (10), 1105–1111. https://doi.org/10.1038/s41563-019-0438-9.

(83) Zhao, C.; Lyu, M.; Bi, C.; Huo, S.; Li, S.; Xue, W. Synthesis of High Ionic Conductivity Li6PS5Cl Solid Electrolyte by Second Sintering Process. *Results Chem* **2022**, *4*, 100468. https://doi.org/10.1016/J.RECHEM.2022.100468.

(84) Liu, G.; Weng, W.; Zhang, Z.; Wu, L.; Yang, J.; Yao, X. Densified Li6PS5Cl Nanorods with High Ionic Conductivity and Improved Critical Current Density for All-Solid-State Lithium Batteries. *Nano Lett* **2020**, *20* (9), 6660–6665. https://doi.org/10.1021/ACS.NANOLETT.0C02489/ASSET/IMAGES/LARGE/NL0C02489_0004.JPEG.

(85) Spencer Jolly, D.; Ning, Z.; Hartley, G. O.; Liu, B.; Melvin, D. L. R.; Adamson, P.; Marrow, J.; Bruce, P. G. Temperature Dependence of Lithium Anode Voiding in Argyrodite Solid-State Batteries. *ACS Appl Mater Interfaces* **2021**, *13* (19), 22708–22716. https://doi.org/10.1021/ACSAMI.1C06706/ASSET/IMAGES/LARGE/AM1C06706_0007.JPEG.

(86) Faka, V.; Agne, M. T.; Till, P.; Bernges, T.; Sadowski, M.; Gautam, A.; Albe, K.; Zeier, W. G. Pressure Dependence of Ionic Conductivity in Site Disordered Lithium Superionic Argyrodite Li 6 PS 5 Br. *Energy Advances* **2023**, *2* (11), 1915–1925. https://doi.org/10.1039/D3YA00424D.

(87) Cronau, M.; Szabo, M.; König, C.; Wassermann, T. B.; Roling, B. How to Measure a Reliable Ionic Conductivity? The Stack Pressure Dilemma of Microcrystalline Sulfide-Based Solid Electrolytes. *ACS Energy Lett* **2021**, *6* (9), 3072–3077. https://doi.org/10.1021/ACSENERGYLETT.1C01299/ASSET/IMAGES/LARGE/NZ1C01299_0005.JPEG.

(88) Wang, Y.; Lim, R.; Larson, K.; Knab, A.; Fontecha, D.; Caverly, S.; Song, J.; Park, C.; Albertus, P.; Rubloff, G. W.; Lee, S. B.; Kozen, A. C. Chemical and Electrochemical Characterization of Hot-Pressed Li6PS5Cl Solid State Electrolyte: Operating Pressure-Invariant High Ionic Conductivity. *ChemSusChem* **2024**, e202400718. https://doi.org/10.1002/CSSC.202400718.

(89) Ohno, S.; Bernges, T.; Buchheim, J.; Duchardt, M.; Hatz, A. K.; Kraft, M. A.; Kwak, H.; Santhosha, A. L.; Liu, Z.; Minafra, N.; Tsuji, F.; Sakuda, A.; Schlem, R.; Xiong, S.; Zhang, Z.; Adelhelm, P.; Chen, H.; Hayashi, A.; Jung, Y. S.; Lotsch, B. V.; Roling, B.; Vargas-Barbosa, N. M.; Zeier, W. G. How Certain Are the Reported Ionic Conductivities of Thiophosphate-Based Solid Electrolytes? An Interlaboratory Study. *ACS Energy Lett* **2020**, *5* (3), 910–915. https://doi.org/10.1021/ACSENERGYLETT.9B02764/ASSET/IMAGES/LARGE/NZ9B02764_0003.JPEG.

(90) Liu, G.; Weng, W.; Zhang, Z.; Wu, L.; Yang, J.; Yao, X. Densified Li6PS5Cl Nanorods with High Ionic Conductivity and Improved Critical Current Density for All-Solid-State Lithium Batteries. *Nano Lett* **2020**, *20* (9), 6660–6665. https://doi.org/10.1021/ACS.NANOLETT.0C02489/SUPPL_FILE/NL0C02489_SI_001.PDF.

(91) Boulineau, S.; Courty, M.; Tarascon, J. M.; Viallet, V. Mechanochemical Synthesis of Li-Argyrodite Li6PS5X (X = Cl, Br, I) as Sulfur-Based Solid Electrolytes for All Solid State Batteries Application. *Solid State Ion* **2012**, *221*, 1–5. https://doi.org/10.1016/J.SSI.2012.06.008.

(92) Rao, R. P.; Adams, S. Studies of Lithium Argyrodite Solid Electrolytes for All-Solid-State Batteries. *physica status solidi (a)* **2011**, *208* (8), 1804–1807. https://doi.org/10.1002/PSSA.201001117.

(93) Boulineau, S.; Courty, M.; Tarascon, J. M.; Viallet, V. Mechanochemical Synthesis of Li-Argyrodite Li6PS5X (X = Cl, Br, I) as Sulfur-Based Solid Electrolytes for All Solid State Batteries Application. *Solid State Ion* **2012**, *221*, 1–5. https://doi.org/10.1016/J.SSI.2012.06.008.

(94) Papakyriakou, M.; Lu, M.; Liu, Y.; Liu, Z.; Chen, H.; McDowell, M. T.; Xia, S. Mechanical Behavior of Inorganic Lithium-Conducting Solid Electrolytes. *J Power Sources* **2021**, *516*, 230672. https://doi.org/10.1016/J.JPOWSOUR.2021.230672.

(95) Liu, C.; Chen, B.; Zhang, T.; Zhang, J.; Wang, R.; Zheng, J.; Mao, Q.; Liu, X. Electron Redistribution Enables Redox-Resistible Li6PS5Cl towards High-Performance All-Solid-State Lithium Batteries. *Angewandte Chemie International Edition* **2023**, *62* (22), e202302655. https://doi.org/10.1002/ANIE.202302655.

(96) Deiseroth, H.-J.; Kong, S.-T.; Eckert, H.; Vannahme, J.; Reiner, C.; Zaiß, T.; Schlosser, M.; Schlosser, M.; Eckert, H.; Vannahme, J. Li 6 PS 5 X: A Class of Crystalline Li-Rich Solids With an Unusually High Li + Mobility**. **2008**, *120*, 767–770. https://doi.org/10.1002/ange.200703900.

(97) Wang, S.; Zhang, Y.; Zhang, X.; Liu, T.; Lin, Y. H.; Shen, Y.; Li, L.; Nan, C. W. High-Conductivity Argyrodite Li 6 PS 5 Cl Solid Electrolytes Prepared via Optimized Sintering Processes for All-Solid-State Lithium-Sulfur Batteries. *ACS Appl Mater Interfaces* **2018**, *10* (49), 42279–42285. https://doi.org/10.1021/ACSAMI.8B15121/ASSET/IMAGES/LARGE/AM-2018-151213_0007.JPEG.

(98) Kim, D. H.; Lee, Y. H.; Song, Y. B.; Kwak, H.; Lee, S. Y.; Jung, Y. S. Thin and Flexible Solid Electrolyte Membranes with Ultrahigh Thermal Stability Derived from Solution-Processable Li Argyrodites for All-Solid-State Li-Ion Batteries. *ACS Energy Lett* **2020**, *5* (3), 718–727. https://doi.org/10.1021/ACSENERGYLETT.0C00251/ASSET/IMAGES/LARGE/NZ0C00251_0005.JPEG.

(99) Liu, G.; Weng, W.; Zhang, Z.; Wu, L.; Yang, J.; Yao, X. Densified Li6PS5Cl Nanorods with High Ionic Conductivity and Improved Critical Current Density for All-Solid-State Lithium Batteries. *Nano Lett* **2020**, *20* (9), 6660–6665.

https://doi.org/10.1021/ACS.NANOLETT.0C02489/ASSET/IMAGES/LARGE/NL0C02489_0004.JPEG.

(100) Xia, Y.; Li, J.; Zhang, J.; Zhou, X.; Huang, H.; He, X.; Gan, Y.; Xiao, Z.; Zhang, W. Yttrium Stabilized Argyrodite Solid Electrolyte with Enhanced Ionic Conductivity and Interfacial Stability for All-Solid-State Batteries. *J Power Sources* **2022**, *543*, 231846. https://doi.org/10.1016/J.JPOWSOUR.2022.231846.

(101) Sun, Z.; Lai, Y.; Lv, N.; Hu, Y.; Li, B.; Jiang, L.; Wang, J.; Yin, S.; Li, K.; Liu, F. Insights on the Properties of the O-Doped Argyrodite Sulfide Solid Electrolytes (Li6PS5- XClOx,X=0-1). *ACS Appl Mater Interfaces* **2021**, *13* (46), 54924–54935. https://doi.org/10.1021/ACSAMI.1C14573/SUPPL_FILE/AM1C14573_SI_001.PDF.

(102) Rao, R. P.; Adams, S. Studies of Lithium Argyrodite Solid Electrolytes for All-Solid-State Batteries. *physica status solidi (a)* **2011**, *208* (8), 1804–1807. https://doi.org/10.1002/PSSA.201001117.

(103) Deiseroth, H. J.; Maier, J.; Weichert, K.; Nickel, V.; Kong, S. T.; Reiner, C. Li7PS6 and Li6PS5X (X: Cl, Br, I): Possible Three-Dimensional Diffusion Pathways for Lithium Ions and Temperature Dependence of the Ionic Conductivity by Impedance Measurements. *Z Anorg Allg Chem* **2011**, *637* (10), 1287–1294. https://doi.org/10.1002/ZAAC.201100158.

(104) Buchberger, D. A.; Garbacz, P.; Słupczyński, K.; Brzezicki, A.; Boczar, M.; Czerwiński, A. Lithium Transport Studies on Chloride-Doped Argyrodites as Electrolytes for Solid-State Batteries. *ACS Appl Mater Interfaces* **2023**, *15* (46), 53417–53428. https://doi.org/10.1021/ACSAMI.3C10857/ASSET/IMAGES/LARGE/AM3C10857_0008.JPEG.

(105) Morino, Y.; Sano, H.; Kawaguchi, S.; Hori, S.; Sakuda, A.; Takahashi, T.; Miyashita, N.; Hayashi, A.; Kanno, R. High-Frequency Impedance Spectroscopic Analysis of Argyrodite-Type Sulfide-Based Solid Electrolyte upon Air Exposure. *Journal of Physical Chemistry C* **2023**, *127* (37), 18678–18683. https://doi.org/10.1021/ACS.JPCC.3C03766/ASSET/IMAGES/LARGE/JP3C03766_0007.JPEG.

(106) Marx, V.; Balke, H. A Critical Investigation of the Unloading Behavior of Sharp Indentation. *Acta Mater* **1997**, *45* (9), 3791–3800. https://doi.org/10.1016/S1359-6454(97)00031-1.

(107) Deng, Z.; Wang, Z.; Chu, I.-H.; Luo, J.; Ong, S. P. Elastic Properties of Alkali Superionic Conductor Electrolytes from First Principles Calculations. *J Electrochem Soc* **2016**, *163* (2), A67–A74. https://doi.org/10.1149/2.0061602JES/XML.

(108) Jackson, I.; Faul, U. H.; Skelton, R. Elastically Accommodated Grain-Boundary Sliding: New Insights from Experiment and Modeling. *Physics of the Earth and Planetary Interiors* **2014**, *228*, 203–210. https://doi.org/10.1016/J.PEPI.2013.11.014.

(109) Baranowski, L. L.; Heveran, C. M.; Ferguson, V. L.; Stoldt, C. R. Multi-Scale Mechanical Behavior of the Li3PS4 Solid-Phase Electrolyte. *ACS Appl Mater Interfaces* **2016**, *8* (43), 29573–29579. https://doi.org/10.1021/ACSAMI.6B06612/ASSET/IMAGES/LARGE/AM-2016-066126_0006.JPEG.

(110) Chen, H.; Zhang, H.; Zhou, Y.; Chen, J.; Huang, X.; Tian, B. Structure-Conduction Correlations in a Chlorine-Rich Superionic Lithium-Argyrodite Solid Electrolyte: A DRT Analysis. *J Power Sources* **2023**, *583*, 233579. https://doi.org/10.1016/J.JPOWSOUR.2023.233579.

(111) Zhao, P.; Guo, Y. Grain Size Effects on Indentation-Induced Defect Evolution and Plastic Deformation Mechanism of Ploycrystalline Materials. *Comput Mater Sci* **2018**, *155*, 431–438. https://doi.org/10.1016/J.COMMATSCI.2018.09.014.

(112) Pharr, G. M.; Herbert, E. G.; Gao, Y. The Indentation Size Effect: A Critical Examination of Experimental Observations and Mechanistic Interpretations. *Annu Rev Mater Res* **2010**, *40* (Volume 40, 2010), 271–292. https://doi.org/10.1146/ANNUREV-MATSCI-070909-104456/CITE/REFWORKS.

(113) Papakyriakou, M.; Lu, M.; Liu, Y.; Liu, Z.; Chen, H.; McDowell, M. T.; Xia, S. Mechanical Behavior of Inorganic Lithium-Conducting Solid Electrolytes. *J Power Sources* **2021**, *516*, 230672. https://doi.org/10.1016/J.JPOWSOUR.2021.230672.

(114) Clark, S.; Bleken, F. L.; Stier, S.; Flores, E.; Andersen, C. W.; Marcinek, M.; Szczesna-Chrzan, A.; Gaberscek, M.; Palacin, M. R.; Uhrin, M.; Friis, J. Toward a Unified Description of Battery Data. *Adv Energy Mater* **2022**, *12* (17), 2102702. https://doi.org/10.1002/AENM.202102702.

(115) Ward, L.; Babinec, S.; Dufek, E. J.; Howey, D. A.; Viswanathan, V.; Aykol, M.; Beck, D. A. C.; Blaiszik, B.; Chen, B. R.; Crabtree, G.; Clark, S.; De Angelis, V.; Dechent, P.; Dubarry, M.; Eggleton, E. E.; Finegan, D. P.; Foster, I.; Gopal, C. B.; Herring, P. K.; Hu, V. W.; Paulson, N. H.; Preger, Y.; Uwe-Sauer, D.; Smith, K.; Snyder, S. W.; Sripad, S.; Tanim, T. R.; Teo, L. Principles of the Battery Data Genome. *Joule* **2022**, *6* (10), 2253–2271. https://doi.org/10.1016/J.JOULE.2022.08.008.

(116) Boaretto, N.; Garbayo, I.; Valiyaveettil-SobhanRaj, S.; Quintela, A.; Li, C.; Casas-Cabanas, M.; Aguesse, F. Lithium Solid-State Batteries: State-of-the-Art and Challenges for Materials, Interfaces and Processing. *J Power Sources* **2021**, *502*, 229919. https://doi.org/10.1016/J.JPOWSOUR.2021.229919.

(117) Wang, C.; Sun, X. The Promise of Solid-State Batteries for Safe and Reliable Energy Storage. *Engineering* **2023**, *21*, 32–35. https://doi.org/10.1016/J.ENG.2022.10.008.

(118) *Winning the Battery Race: How the United States Can Leapfrog China to Dominate Next-Generation Battery Technologies | Carnegie Endowment for International Peace*. https://carnegieendowment.org/research/2024/10/winning-the-battery-race-how-the-united-states-can-leapfrog-china-to-dominate-next-generation-battery-technologies?lang=en&center=europe (accessed 2025-03-15).

(119) Jacobsson, T. J.; Hultqvist, A.; García-Fernández, A.; Anand, A.; Al-Ashouri, A.; Hagfeldt, A.; Crovetto, A.; Abate, A.; Ricciardulli, A. G.; Vijayan, A.; Kulkarni, A.; Anderson, A. Y.; Darwich, B. P.; Yang, B.; Coles, B. L.; Perini, C. A. R.; Rehermann, C.; Ramirez, D.; Fairen-Jimenez, D.; Di Girolamo, D.; Jia, D.; Avila, E.; Juarez-Perez, E. J.; Baumann, F.; Mathies, F.; González, G. S. A.; Boschloo, G.; Nasti, G.; Paramasivam, G.; Martínez-Denegri, G.; Näsström, H.; Michaels,

H.; Köbler, H.; Wu, H.; Benesperi, I.; Dar, M. I.; Bayrak Pehlivan, I.; Gould, I. E.; Vagott, J. N.; Dagar, J.; Kettle, J.; Yang, J.; Li, J.; Smith, J. A.; Pascual, J.; Jerónimo-Rendón, J. J.; Montoya, J. F.; Correa-Baena, J. P.; Qiu, J.; Wang, J.; Sveinbjörnsson, K.; Hirselandt, K.; Dey, K.; Frohna, K.; Mathies, L.; Castriotta, L. A.; Aldamasy, M. H.; Vasquez-Montoya, M.; Ruiz-Preciado, M. A.; Flatken, M. A.; Khenkin, M. V.; Grischek, M.; Kedia, M.; Saliba, M.; Anaya, M.; Veldhoen, M.; Arora, N.; Shargaieva, O.; Maus, O.; Game, O. S.; Yudilevich, O.; Fassl, P.; Zhou, Q.; Betancur, R.; Munir, R.; Patidar, R.; Stranks, S. D.; Alam, S.; Kar, S.; Unold, T.; Abzieher, T.; Edvinsson, T.; David, T. W.; Paetzold, U. W.; Zia, W.; Fu, W.; Zuo, W.; Schröder, V. R. F.; Tress, W.; Zhang, X.; Chiang, Y. H.; Iqbal, Z.; Xie, Z.; Unger, E. An Open-Access Database and Analysis Tool for Perovskite Solar Cells Based on the FAIR Data Principles. *Nature Energy 2021 7:1* **2021**, *7* (1), 107–115. https://doi.org/10.1038/s41560-021-00941-3.

(120) Randau, S.; Weber, D. A.; Kötz, O.; Koerver, R.; Braun, P.; Weber, A.; Ivers-Tiffée, E.; Adermann, T.; Kulisch, J.; Zeier, W. G.; Richter, F. H.; Janek, J. Benchmarking the Performance of All-Solid-State Lithium Batteries. *Nature Energy 2020 5:3* **2020**, *5* (3), 259–270. https://doi.org/10.1038/s41560-020-0565-1.

(121) Puls, S.; Nazmutdinova, E.; Kalyk, F.; Woolley, H. M.; Thomsen, J. F.; Cheng, Z.; Fauchier-Magnan, A.; Gautam, A.; Gockeln, M.; Ham, S.-Y.; Hasan, M. T.; Jeong, M.-G.; Hiraoka, D.; Kim, J. S.; Kutsch, T.; Lelotte, B.; Minnmann, P.; Miß, V.; Motohashi, K.; Nelson, D. L.; Ooms, F.; Piccolo, F.; Plank, C.; Rosner, M.; Sandoval, S. E.; Schlautmann, E.; Schuster, R.; Spencer-Jolly, D.; Sun, Y.; Vishnugopi, B. S.; Zhang, R.; Zheng, H.; Adelhelm, P.; Brezesinski, T.; Bruce, P. G.; Danzer, M.; El Kazzi, M.; Gasteiger, H.; Hatzell, K. B.; Hayashi, A.; Hippauf, F.; Janek, J.; Jung, Y. S.; McDowell, M. T.; Meng, Y. S.; Mukherjee, P. P.; Ohno, S.; Roling, B.; Sakuda, A.; Schwenzel, J.; Sun, X.; Villevieille, C.; Wagemaker, M.; Zeier, W. G.; Vargas-Barbosa, N. M. Benchmarking the Reproducibility of All-Solid-State Battery Cell Performance. *Nature Energy 2024 9:10* **2024**, *9* (10), 1310–1320. https://doi.org/10.1038/s41560-024-01634-3.

(122) The Path to Accurate Reporting. *Nature Energy 2024 9:10* **2024**, *9* (10), 1175–1176. https://doi.org/10.1038/s41560-024-01663-y.